PHYSICAL REVIEW B **110**, 075149 (2024)

Energy diffusion in weakly interacting chains with fermionic dissipation assisted operator evolution

En-Jui Kuo,[1,2,3] Brayden Ware,[2,3] Peter Lunts,[4,2] Mohammad Hafezi,[1,2,3] and Christopher David White[3]
[1]*Department of Physics, University of Maryland, College Park, Maryland 20742, USA*
[2]*Joint Quantum Institute, NIST/University of Maryland, College Park, Maryland 20742, USA*
[3]*Joint Center for Quantum Information and Computer Science, University of Maryland, College Park, Maryland 20742, USA*
[4]*Department of Physics, Harvard University, Cambridge, Massachusetts 02138, USA*

(Received 12 December 2023; revised 15 June 2024; accepted 17 June 2024; published 26 August 2024)

Interacting lattice Hamiltonians at high temperature generically give rise to energy transport governed by the classical diffusion equation; however, predicting the rate of diffusion requires numerical simulation of the microscopic quantum dynamics. For the purpose of predicting such transport properties, computational time evolution methods must be paired with schemes to control the growth of entanglement to tractably simulate for sufficiently long times. One such truncation scheme—dissipation-assisted operator evolution (DAOE)—controls entanglement by damping out components of operators with large Pauli weight. In this paper, we generalize DAOE to treat fermionic systems. Our method instead damps out components of operators with large fermionic weight. We investigate the performance of DAOE, the new fermionic DAOE (FDAOE), and another simulation method, density matrix truncation (DMT), in simulating energy transport in an interacting one-dimensional Majorana chain. The chain is found to have a diffusion coefficient scaling like interaction strength to the fourth power, contrary to naive expectations based on Fermi's Golden rule—but consistent with recent predictions based on the theory of *weak integrability breaking*. In the weak interaction regime where the fermionic nature of the system is most relevant, FDAOE is found to simulate the system more efficiently than DAOE.

DOI: 10.1103/PhysRevB.110.075149

I. INTRODUCTION

Simulating transport in strongly interacting systems is a core challenge in quantum many-body physics, with implications from strange metal physics in cuprates and iron pnictides [1–7] to heavy-ion collisions [8–12]. Because complete numerical solution of a particular Hamiltonian is generally feasible only for small systems, transport simulations rely on approximate numerical methods. But transport is understood in terms of two largely separate languages, depending on the degree of interaction: nearly free fermion [13] (and nearly Bethe ansatz integrable [14–20]) systems can be understood in terms of Boltzmann theory, while strongly interacting systems are understood in terms of an increasingly detailed theoretical understanding of how thermalization and hydrodynamics emerge from unitary microscopic dynamics [21–25]. Cold-atom experiments highlight this gap: they can tune from free-fermion to strongly interacting by tuning a Feshbach resonance [26,27] or changing the geometry of a quasi-one-dimensional ladder geometry [28]. At the same time, progress in analytical and numerical treatment of systems showing Bethe ansatz integrability [29], weakly broken Bethe ansatz integrability [14–20], and strong integrability-breaking interactions [22–25,30,31] suggests that quantum simulation may not be necessary, at least for one-dimensional (1D) systems. But classical methods have not been shown to work in the crossover regime between weak interaction, tractable with Boltzmann methods, and strong interaction, tractable with recent methods. We present a matrix product operator method for simulating transport in one-dimensional high-temperature quantum systems that is suitable for that regime; it can treat both nearly-free-fermion and strongly interacting Hamiltonians.

Existing methods for strongly interacting systems become impractical at weak interaction, lack a perturbatively small simulation parameter controlling deviation from the exact dynamics, or both. Density matrix truncation (DMT) [30] works in all ranges of integrability [32–35], but it is nontrivial to implement and difficult to analyze. It is also uncontrolled: like many matrix product operator methods, one checks the accuracy of DMT simulations by looking for convergence in bond dimension, but for large systems, practical bond dimensions cannot approach the bond dimensions required to exactly simulate the state. Indeed, the premise of DMT, applied to systems that thermalize, is that most of the operator can be discarded, because it consists of physically irrelevant correlations.

Dissipation-assisted operator evolution (DAOE) [31] offers a controllable approximation to a system's dynamics with a straightforward matrix product operator implementation—but it is not suitable for systems near free-fermion integrability. DAOE modifies the Heisenberg dynamics to include an artificial dissipation-like superoperator with a parametrically small rate γ. Just as depolarizing noise with rate γ reduces the amplitude of operators with Pauli weight (number of nontrivial Pauli strings) l at a rate γl, the artificial dissipation reduces the amplitude of operators with Pauli weight $l > l_*$ at a rate $\gamma(l - l_*)$. Figure 1 (top) shows a cartoon of this process. It therefore reduces the state's complexity by decreasing the amplitude of long operators, without changing local operators. Because the long operators on which DAOE acts most strongly are—

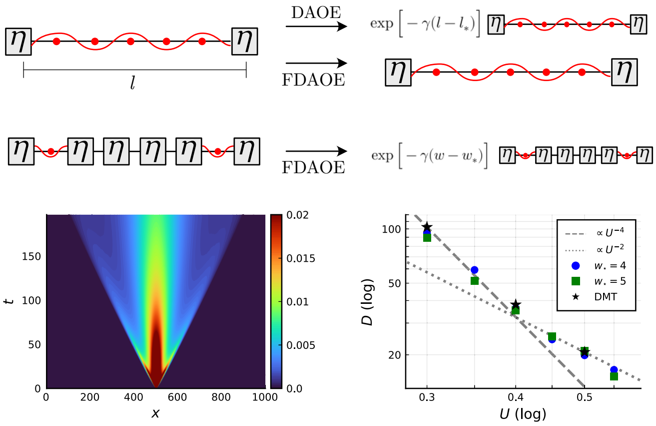

FIG. 1. Top: dissipation-assisted operator evolution (DAOE) compared with fermionic dissipation-assisted operator evolution (FDAOE). Where DAOE reduces widely separated quadratic fermion operators almost to zero, FDAOE leaves them untouched; FDAOE depolarizes operators with fermion weight greater than some cutoff w_*. Bottom left: energy density as a function of position x and time t in the nearly-free Majorana model (2) at $U = 0.3$, simulated in FDAOE. Bottom right: finite-time estimates of the diffusion coefficient D. At small U, these estimates are consistent with $D \propto U^{-4}$, but not $D \propto U^{-2}$; the power is due to weak integrability breaking.

for chaotic, strongly interacting systems—unimportant to the finite-time dynamics [23], one can think of the DAOE dissipation superoperator as perturbatively modifying the local dynamics. DAOE results at small but finite γ can therefore be extrapolated to the unitary $\gamma = 0$ dynamics of interest, in a manner similar to zero-noise extrapolation [36,37].

But when the system is not strongly interacting, the high-weight operators affected by DAOE can be important to local dynamics, and the dissipation is not a small perturbation. In such a system, momentum occupation numbers like $c_k^\dagger c_k$ (where c_k is a fermion momentum mode annihilation operator) are nearly conserved quantities, so modifying them renders any description of the system's hydrodynamics unfaithful. But simple long-range fermion operators like $c_k^\dagger c_k$ have large weight when written in Pauli matrices, due to Jordan-Wigner strings, so the artificial dissipation causes them to decay rapidly; this artificial decay will dominate the system's apparent transport properties.

We modify DAOE to respect the fermionic structure underlying weakly interacting 1D systems; we call the resulting method *fermionic DAOE* (FDAOE). FDAOE preserves quadratic fermion operators like $c_k^\dagger c_k$ while dissipating operator components consisting of products of large numbers of fermion operators. Like DAOE, it is efficient and easy to implement due to its compact matrix product operator representation. This allows us to study both strongly and weakly nonintegrable fermionic models using the same controlled and intuitive method.

We test FDAOE and a prior method, DMT, on a model displaying *weak integrability breaking* [38]. In such models, an integrability-breaking perturbation is added to an integrable (in our case free-fermion) model. At leading order, the perturbation dresses the integrable system's conserved quantities, giving ballistic transport; beyond leading order it scatters those quantities, giving diffusive transport. Reference [38] predicts relaxation times $\sim U^{2+2\nu}$, where ν is a positive integer for perturbations that exhibit weak integrability breaking and 0 for perturbations that do not.

We find that both FDAOE and DMT capture infinite-temperature dynamical correlation functions of energy density in such a system on short and intermediate timescales. Both methods are limited by rapid growth of the patch of the system they must simulate: on timescales short compared with the scattering time, which is itself not short, energy density spreads nearly ballistically and one must simulate systems of diameter $\propto vt$. Although FDAOE and DMT both allow simulation at bond dimensions ∼64–128, this spread still gives cost per time step $\sim vt$ and total simulation cost $\sim t^2$. FDAOE is additionally limited by SVD error.

Both methods give finite-time energy density diffusion coefficients consistent with $D \sim U^{-4}$ but not the simple Fermi golden rule $D \sim U^{-2}$ expected from ordinary integrability breaking. This U^4 scaling confirms that weak integrability breaking governs the system's dynamics not only at times short compared to interaction and hopping, where [38] worked, but on long times as well.

The paper is organized as follows. In Sec. II we discuss the model used for benchmarking, we give a brief overview of weak integrability breaking, and we discuss the quantities of interest. In Sec. III we review DAOE, and we present our method FDAOE and describe simulations and simulation costs. In Sec. IV we present the results and discuss the performance of FDAOE compared to DAOE, and in Sec. V we conclude.

II. MODEL AND QUANTITIES OF INTEREST

A. Model

We study the infinite-temperature energy transport of an interacting Majorana chain

$$H = \sum_n i\eta_n\eta_{n+1} - U\sum_n \eta_{n-1}\eta_n\eta_{n+1}\eta_{n+2}. \qquad (1)$$

We work in the units where the quadratic "hopping" term has been set to 1. We chose this model by starting with the simplest example of a 1D free-fermion model with energy conservation but without particle number conservation and adding the most natural fermion parity-conserving interaction. (The low-energy properties of this Hamiltonian were previously studied in Ref. [39].)

This Hamiltonian is equivalent to the spin-1/2 Hamiltonian

$$H = \sum_n \sigma_n^x\sigma_{n+1}^x + \sigma_n^z + U\left(\sigma_n^x\sigma_{n+2}^x + \sigma_n^z\sigma_{n+1}^z\right) \qquad (2)$$

by Jordan-Wigner transformation. We work with the spin-language Hamiltonian (2).

We choose a model (1) with only a single conserved quantity, the energy density, so we can study transport in the simplest possible setting. We analyze our simulations through the lens of a single-component diffusion equation [22,24,31,35,40,41].

We do not expect our simulation methods to break down in systems with multiple conserved quantities. But when a system has multiple conserved quantities, nonlinear interactions between the conserved quantities can contribute significantly to transport properties, so going beyond the linear diffusion equation is necessary to analyze such systems [42]. Nonlinear effects can also appear in systems with a single conserved quantity [42–44], but previous numerical simulations in spin chains with only energy conservation have not detected significant nonlinear contributions to energy transport [35]. In this work, we also do not detect significant nonlinear contributions.

We have chosen an interaction that is not integrable using the Bethe ansatz. Bethe ansatz integrable systems have an infinite hierarchy of additional conserved quantities beyond energy density. The methods we use throughout this paper are designed to truncate irrelevant information while preserving the behavior of densities of conserved quantities, which are short-range or few-fermion operators like the energy density. So we would not expect them to be appropriate for Bethe-ansatz integrable systems which have conserved quantities with arbitrarily large operator size: see Appendix B in Ref. [31] and Ref. [45] for more discussion of this point.

While the Hamiltonian we study in this paper has no additional conserved quantities for nonzero U, we wish to study transport in a regime of small U, in the neighborhood of the free-fermion point. At this free point, the model has many additional conserved quantities that are quadratic in the fermion operators. Such quantities are almost conserved when U is small but nonzero, and thus they may contribute significantly to long-time dynamics. Prior studies using tensor network algorithms have not attempted to predict transport properties in the nearly free-fermion regime of 1D chains, and it is not clear whether such methods would succeed for this purpose. On the other hand, FDAOE is designed specifically to preserve information about the low-fermion weight quantities that are almost conserved in the small-U regime.

B. Weak integrability breaking

In the regime of weak interactions, transport can sometimes be studied using simpler means, with the transport coefficients computed perturbatively in linear response using the Kubo formula, avoiding the need for simulations of operator dynamics.

However, we expect that the model studied in this paper evades a simple perturbative analysis, as it exhibits *weak integrability breaking* [38]. The core prediction of weak integrability breaking for this model is that scattering times do not scale as predicted by Fermi's golden rule, with the square of the perturbation strength U, but with a different power-law scaling. This is due to a hidden nonlocal map that approximately transforms the Hamiltonian into a free-fermion Hamiltonian, which we describe below. This implies that in the perturbative calculation, current-current correlators need to be computed to a higher order than expected to obtain a finite result (in this case, fourth order rather than second order in U). The simulation methods in this paper are able to recover the unusual scaling with U without any explicit knowledge of the weak integrability breaking.

Weak integrability breaking starts from the elementary observation that if $n_\alpha^{(0)}$ is a conserved quantity of some Hamiltonian H_0, then

$$n'_\alpha = e^{i\lambda X} n_\alpha^{(0)} e^{-i\lambda X}, \tag{3}$$

where X is a Hermitian operator, is a conserved quantity of

$$H' = e^{i\lambda X} H_0 e^{-i\lambda X}. \tag{4}$$

But for small λ, this H' is not so far from

$$H = H_0 + i\lambda[X, H_0] = H' + O(\lambda^2). \tag{5}$$

When the initial Hamiltonian H_0 is chosen to be an integrable Hamiltonian with conserved quantities $\{n_\alpha^{(0)}\}$, the perturbed quantities

$$n_\alpha = n_\alpha^{(0)} + i\lambda\big[X, n_\alpha^{(0)}\big] = n'_\alpha + O(\lambda^2) \tag{6}$$

are nearly conserved. That is,

$$[H, n_\alpha] \propto \lambda^2, \tag{7}$$

in contrast to a generic perturbation that leads to matrix elements $[H_0 + V, n_\alpha^{(0)}] \propto \lambda$. Indeed, by keeping higher commutators in (5) and (6), one can engineer nearly conserved quantities with arbitrarily slow decays $[H, n_\alpha] \propto \lambda^{2k}$.

The challenge is to find generators X that produce a local perturbation V of interest via $V = i[X, H_0]$, which is only possible for select perturbations V. Reference [38] systematically constructs a family of nonlocal generators X that produce local perturbations when the unperturbed Hamiltonian H_0 is free-fermion or Bethe ansatz integrable. Specifically, the examples of generators X that they construct are bilocal combinations of conserved densities $n_\alpha^{(0)}$ of H_0 and their corresponding current operators.

For our purposes, we only need to consider one such generator X for a free Majorana chain that produces the interaction term of Eq. (1). The appropriate generator is constructed from a nonlocal combination of the energy density and energy current density operators of the unperturbed Hamiltonian:

$$\begin{aligned}
X &= \sum_{m<n} \big\{\varepsilon_m^{(0)}, j_n^{(0)}\big\} + \frac{1}{2}\sum_n \big\{\varepsilon_n^{(0)}, j_n^{(0)}\big\},\\
\varepsilon_n^{(0)} &= \sigma_n^x \sigma_{n+1}^x + \frac{1}{2}\big(\sigma_n^z + \sigma_{n+1}^z\big),\\
j_n^{(0)} &= \sigma_n^x \sigma_{n+1}^y - \sigma_n^y \sigma_{n+1}^x.
\end{aligned} \tag{8}$$

One can check (with some purely mechanical effort) that the interacting Hamiltonian in Eq. (1) satisfies

$$H = H_0 + i\lambda[X, H_0] \tag{9}$$

with

$$H_0 = \sum_j i\eta_j \eta_{j+1} \tag{10a}$$

and $\lambda = U/4$.

C. Quantities of interest

If a system thermalizes, it approaches local thermal equilibrium: after a short time, it can be described by a density matrix

$$\rho(t) \propto \exp\left[-\sum_x \beta_x(t)\varepsilon_x\right], \tag{11}$$

where $\beta_x(t)$ is a smoothly varying space- and time-dependent inverse temperature, and ε_x is the energy density. (We consider systems with only one conserved quantity, the energy density; a discussion of systems with more than one conserved quantity would proceed analogously.) This state is specified entirely by the energy expectation values $\mathrm{tr}\rho(t)\varepsilon_x$. For times longer than the initial thermalization time, the energy density correlation function

$$C(x,t) = \langle \varepsilon_x(t)\varepsilon_0(0)\rangle \tag{12}$$

therefore captures the whole dynamics in this long-time regime, and the extent to which it deviates from a gradient-expansion prediction from (11) diagnoses the local thermalization process.

On timescales long compared with the local thermalization time, the system's dynamics are given by the continuity equation and a gradient expansion of the state (11); the result is

$$\begin{aligned} \partial_t \varepsilon &= \partial_x j, \\ \partial_t j &= D\partial_x \varepsilon + \cdots . \end{aligned} \tag{13}$$

To the extent that the system is described by the leading-order term in the gradient expansion (13), the energy density correlation function is the Gaussian $C(x,t) \propto \exp[-x^2/4Dt]$.

But real systems are only described by (13) on timescales long compared to the microscopic thermalization timescale. To characterize the correlation function $C(x,t)$ at short or intermediate timescales, we can measure the degree to which it spreads away from the initial point $x = 0$ to introduce a time-dependent diffusion coefficient. The degree of spread is the mean-squared displacement

$$V(t) = \frac{1}{\nu}\left[\sum_x x^2 C(x,t) - \left(\sum_x xC(x,t)\right)^2\right], \tag{14}$$

where ν is a (time-independent) normalization

$$\nu = \sum_x C(x,t) = \sum_x C(x,0). \tag{15}$$

The time-dependent diffusion coefficient is

$$D(t) = \frac{1}{2}\frac{d}{dt}V(t). \tag{16}$$

If the system is diffusive, then in the long-time limit its dynamics approaches the diffusion equation (13) with

$$D = \lim_{t\to\infty} D(t). \tag{17}$$

We estimate $D(t)$ by a numerical derivative of the mean-squared displacement $V(t)$.

III. METHOD: FERMION DISSIPATION ASSISTED OPERATOR EVOLUTION

A. Intuition and superoperator

Dissipation assisted operator evolution [31] intersperses unitary time evolution with a dissipation superoperator that reduces the amplitude on high-weight Pauli strings. That dissipation superoperator is

$$\mathcal{D}_{l_*,\gamma}[\mathcal{S}] = \left\{\begin{matrix} \mathcal{S} & \text{if } l_\mathcal{S} \leqslant l_* \\ e^{-\gamma(l_\mathcal{S}-l_*)}\mathcal{S} & \text{if } l_\mathcal{S} > l_* \end{matrix}\right\}, \tag{18}$$

where $\mathcal{S}$ is a Pauli string and $l_\mathcal{S}$ is the *Pauli weight* of $\mathcal{S}$, or the number of nontrivial Pauli operators in $\mathcal{S}$. In the $l_* = 0$ limit, this reduces to a depolarizing channel, hence the name "dissipation superoperator"; from the point of view of DMT [30] or operator size truncated dynamics [24,35], it is a soft truncation on long operators. When the dynamics of long operators is chaotic, the details of the dynamics of long operators does not affect local dynamical correlation functions [23,24], and for $l_* \gg 1$ the superoperator (18) modifies the local dynamics only by modifying the rate at which the amplitude escapes from short operators to long operators.

But for many models of interest, the dynamics of long operators is not chaotic, and the DAOE dissipation superoperator (18) dramatically changes operators of interest. In a system of weakly interacting fermions like (1), a momentum mode such as

$$n_k^{(0)} = \frac{1}{L}\sum_{m<n} \eta_m\eta_n \sin(n-m)k \tag{19}$$

is a conserved quantity of the noninteracting part, and the system's evolution is governed by the dynamics of these momentum modes, together with scattering between them. After Jordan-Wigner transformation, the term $\eta_m\eta_n$ picks up a Jordan-Wigner string between m and n, so it has Pauli weight $l_{\eta_m\eta_n} = m - n + 1$. The DAOE superoperator projects out operators with Pauli weight $l_\mathcal{S} \gtrsim l_* + \gamma^{-1}$, so it truncates the momentum occupation number to the range $l_* + \gamma^{-1}$. Because it changes the conserved quantities of the free model, one expects it to drastically change the transport properties of the interacting model.

In fermionic dissipation assisted operator evolution (FDAOE), we replace the Pauli weight $l_\mathcal{S}$ in the DAOE dissipation superoperator (18) by a fermion weight superoperator. To write the fermion weight superoperator, first represent each Pauli matrix by two Majorana fermion operators

$$\begin{aligned} \sigma_n^x &= \eta_{2n+1}\left[\prod_{m\geqslant n+1} i\eta_{2m}\eta_{2m+1}\right], \\ \sigma_n^y &= \eta_{2n}\left[\prod_{m\geqslant n+1} i\eta_{2m}\eta_{2m+1}\right], \\ \sigma_n^z &= -i\eta_{2n}\eta_{2n+1}. \end{aligned} \tag{20}$$

These Majorana operators form a Hermitian, orthogonal basis for the space of operators, so we can define our Majorana dissipation superoperator by its action on them: if η_J is a product of Majorana operators on the sites J,

$$\eta_J = \prod_{j\in J}\eta_j, \tag{21}$$

then

$$\mathcal{M}_{w_*,\gamma}[\eta_J] = \begin{cases} \eta_J, & w_{\eta_J} \leqslant w_*, \\ e^{-\gamma(w_{\eta_J}-w_*)}\eta_J, & w_{\eta_J} > w_*, \end{cases} \tag{22}$$

with

$$w_{\eta_J} = |J|. \tag{23}$$

All of the terms in the momentum mode $n_k^{(0)}$ of (19) have Majorana weight 2, so for $w_* \geqslant 2$ and any γ,

$$\mathcal{M}_{w_*,\gamma}\big(n_k^{(0)}\big) = n_k^{(0)}. \tag{24}$$

Unlike DAOE, therefore, FDAOE preserves the conserved quantities of the noninteracting Hamiltonian.

The FDAOE superoperator (22) has an MPO representation with bond dimension $w_* + 2$ when represented by its action on the Pauli basis related to the Majorana operators by the Jordan-Wigner transformation, Eq. (20). We give the MPO explicitly in Appendix A, but we outline the construction here. As in the case of the DAOE superoperator described in Ref. [31], the MPO representation utilizes a constant rank-4 tensor, which we denote as $W_{ab}^{nn'}$, with the upper indices n, n' taking values in the local Pauli operator basis $\{I, X, Y, Z\}$. As the FDAOE superoperator is diagonal in the basis of operators that consist of products of Majorana operators, it is also diagonal in the basis of Pauli strings; thus, the only nonzero matrix elements occur in the form W_{ab}^{II}, W_{ab}^{XX}, W_{ab}^{YY}, or W_{ab}^{ZZ}. The virtual indices a, b take values in the set $\{0, 1, \dots, w^* - 1\} \cup \{(w^*, +), (w^*, -)\}$, which track the total fermionic operator weight as measured from the left end of the chain to the bond in question until it reaches w^*, and the fermion parity afterwards. Within each Pauli string, the additional fermionic weight represented by the presence of an X or Y is always 1 and always flips the fermion parity, which is tracked by the virtual index. Consequently, W_{ab}^{XX} and W_{ab}^{YY} are zero unless $a < w^*$ and $b = a + 1$ or $a = (w^*, \pm)$ and $b = (w^*, \mp)$. The weights associated with I and Z, however, are context-dependent; alone, they correspond to weights 0 and 2, respectively, but within a Jordan-Wigner string they correspond to weights 2 and 0, swapping roles. The presence of a Jordan-Wigner string is locally accessible as the parity of the MPO virtual index a. In addition to tracking the fermion weight, the MPO tensor applies a decay factor of $e^{-\gamma}$ for each unit of additional fermion weight beyond w^*. Finally, the tensors are contracted on the left and right ends with the vectors $v_L = (1, 0, \dots, 0)$ and $v_R = (1, 1, \dots, 1)$; this ensures the virtual index starts tracking the fermion weight from weight 0 on the left end of the chain and allows all values of fermion weight on the right end. Explicit expressions for the MPO tensors that meet these conditions are given in Appendix A.

The MPO can be written in terms of tensors that respect an on-site spin or charge $U(1)$; we give details in Appendix A.

B. Computing dynamical correlation functions

We seek to measure dynamical correlation functions

$$\langle \varepsilon_x(t)\varepsilon_0(0)\rangle = \operatorname{tr}(\varepsilon_x e^{-i\mathcal{L}t}[\varepsilon_0]), \tag{25}$$

where $\mathcal{L}$ is the Liouvillian generated by $\mathcal{L}[\cdot] = -i[H, \cdot]$ and where ε_x is the energy density, chosen as a parity symmetric operator that produces H when summed over sites. [ε_x is the energy density of the interacting Hamiltonian, as opposed to the energy density $\varepsilon_x^{(0)}$ of the noninteracting Hamiltonian used in Eq. (8).] Explicitly, we represent ε_x as

$$\begin{aligned}\varepsilon_x = {}& \frac{1}{3}\big(\sigma_x^z + \sigma_{x+1}^z + \sigma_{x+2}^z\big) + \frac{1}{2}\big(\sigma_x^x\sigma_{x+1}^x + \sigma_{x+1}^x\sigma_{x+2}^x\big)\\ &+ \frac{U}{2}\big(\sigma_x^z\sigma_{x+1}^z + \sigma_{x+1}^z\sigma_{x+2}^z\big) + U\big(\sigma_x^x\sigma_{x+2}^x\big).\end{aligned} \tag{26}$$

To measure $\langle \varepsilon_x(t)\varepsilon_0(0)\rangle$, we time-evolve the initial operator ε_0 by the Trotterization of that Liouvillian, interspersed with applications of the FDAOE MPO.

In the limit of large bond dimension, the dominant cost is truncation after MPO application. Since the FDAOE MPO has bond dimension $w_* + 2$, an exact truncation has cost

$$\sim [d^2\chi(w_* + 2)]^3 \tag{27}$$

per bond, where d is the physical on-site Hilbert space dimension [e.g., $d = 2$ for a spin-1/2 Hamiltonian like (2)]. This cost comes about because the exact truncation requires two sweeps, the first to put $\mathcal{M}_{w_*,\gamma} \circ e^{-i\mathcal{L}t}[\varepsilon_0]$ in canonical form and the second to do the truncation. Switching to a so-called "zip-up" truncation, in which one truncates at each site immediately after applying the MPO tensor, reduces the cost to

$$\sim (w_* + 2)[d^2\chi]^3 \tag{28}$$

per bond at the cost of some imprecision [46,47].

The cost of the whole calculation can further be reduced by noting that $e^{-i\mathcal{L}t}[\varepsilon_0]$ acts as the identity outside a light cone of diameter $\sim 2vt$ for some speed v. Both the unitary dynamics and the FDAOE MPO $\mathcal{M}_{w_*}$ act trivially outside that light cone. So the cost of an MPO application at simulation time t generically grows with t: it is

$$\sim (w_* + 2)d^6 \sum_x \chi(x, t)^3 \sim d^6(w_* + 2)\chi(t)^3 2vt, \tag{29}$$

where we write $\chi(x, t)$ for the bond dimension at site x and some site t, and $\chi(t)$ for a typical magnitude at time t. The memory requirements are

$$\sim (2vt)d^6\chi(t)^2. \tag{30}$$

C. Simulation parameters

We use a fourth-order Trotter decomposition; specifically, we use the three-term formula recommended by Ref. [48] that consists of 21 layers of three-site gates for each time step. The size of the time steps is $dt = 0.1$ throughout the paper. The FDAOE MPO is applied after each time step.

After each Trotter gate and during zip-up MPO application, we discard the smallest singular values s_α such that [49]

$$\sum_{\alpha\ \text{discarded}} s_\alpha^2 < \epsilon\left[\sum_\beta s_\beta^2\right], \tag{31}$$

where ϵ is the SVD truncation error.

In Appendix C we discuss convergence in the cutoff ϵ and the magnitude of the noise in the numerical derivative $D(t)$ (cf. Fig. 2). We empirically find that truncating singular values causes noise in $D(t)$ of magnitude

$$\Delta t_{\text{pred}} \sim \sqrt{\epsilon}\, V(t), \tag{32}$$

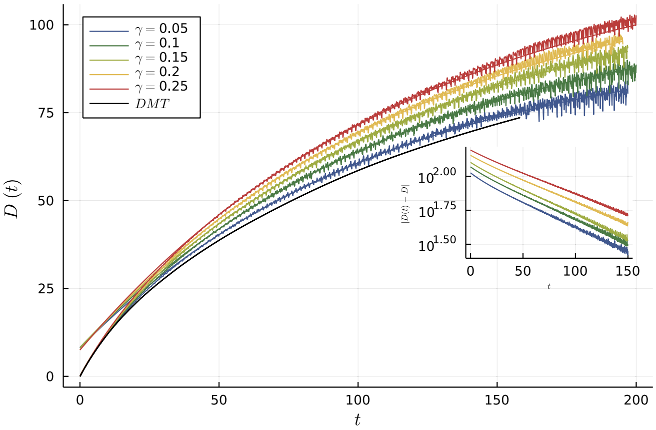

FIG. 2. Diffusion coefficient $D(t)$ as a function of time for the nearly free Majorana model of Sec. II at interaction $U = 0.3$. $D(t)$ is estimated via Eq. (16) using FDAOE at $w_* = 5$ and a range of artificial dissipations γ (colored lines), and DMT at bond dimension 256 and Trotter step 0.125 (black line). (See Appendix D for DMT convergence data.) The noise in the FDAOE $D(t)$ is due to an SVD cutoff $\epsilon = 10^{-8}$ (see Appendix C). For plots of other U, see Fig. 7.

and we give a heuristic argument for why the noise should have that form. We also empirically find that the magnitude of the noise gives a reasonable estimate of the convergence error in ϵ.

The DMT simulations are run at Trotter step $dt = 0.125$ and a fixed bond dimension cap $\chi = 256$; we discuss convergence in bond dimension (and other details of the DMT simulations) in Appendix D.

IV. RESULTS

Figure 2 shows $D(t)$ in the nearly free Majorana model of Sec. II at interaction $U = 0.3$, estimated by taking the numerical derivative of FDAOE simulations of $\langle \varepsilon_x(t)\varepsilon_0(0)\rangle$. The simulations are limited to times $t \lesssim 200$ by the computational cost, which grows with time as the light cone of $\varepsilon_x(t)$ grows. Each $D(t)$ shows high-frequency noise; this is noise is controlled by the SVD truncation cutoff, here $\epsilon = 10^{-8}$ (cf. Appendix C).

After an initial transient behavior, $D(t)$ is described by exponential decay to a long-time limit

$$D(t) = D - Ae^{-t/\tau}. \tag{33}$$

Figure 2 (inset) shows $|D(t) - D|$ in FDAOE simulations, where D is extracted by fitting FDAOE $D(t)$ to the form (33). The result appears exponential over the range of our simulations, although that range is small [covering only a factor of about 3 in decay of $|D(t) - D|$ for $U = 0.3$]. Figure 3 shows the current-current correlator

$$\frac{1}{L}\langle J(t)J(0)\rangle \propto \frac{d}{dt}D(t) \tag{34}$$

in DMT simulations for $U = 0.3, 0.4, 0.5$. (See Appendix D for details of the DMT simulations, including convergence testing, Trotterization, and the definition of the current operator. Note that the current operator corresponds to a different definition of energy density, for reasons of convenience in

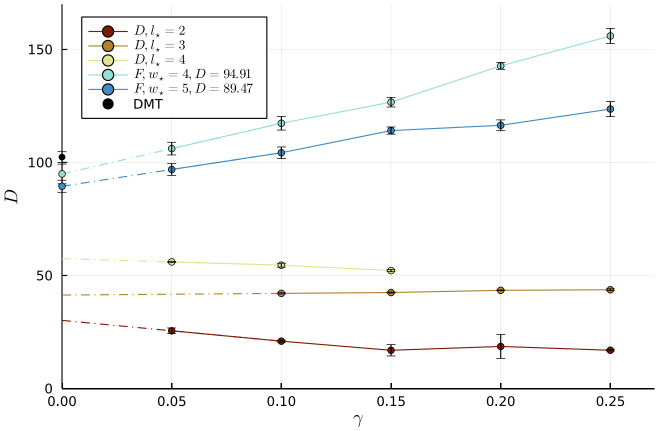

FIG. 3. Current-current correlator in DMT simulations across interaction strengths U (solid lines), together with a single-exponential fit to the $t > 25$ data. In each case, the correlator displays a long-time exponential decay, supporting our choice of fit form (33) for the diffusion coefficient. (We cannot rule out power-law behavior at longer times, especially for $U = 0.3$, which displays less than a decade of decay over the time simulated.)

analytical calculations; this explains the difference in transient early-time behavior.) For each U the current-current correlator displays an early-time transient decay followed by a long-time exponential decay. For $U = 0.5$ this decay covers approximately two orders of magnitude, but for $U = 0.3$ it covers less than a decade. As in Ref. [35], we cannot rule out that the system displays long-time tails, but we expect that if they exist their coefficients are small.

To characterize how the system's long but finite-time behavior depends on U, we fit to the form (33) for U-dependent time windows and consider the "asymptotic" diffusion coefficient D; if the long-time tails are small or nonexistent, this D will match the system's true diffusion coefficient. We fit on time windows $15/U = t_{\min} \leqslant t \leqslant t_{\max} = 30/U$; this form is chosen by eye to avoid both the early-time nonexponential behavior and late-time noise. The window choice is fairly arbitrary. To characterize how the window choice affects the fit, we take end times $t_{\max} = 30/U - 10, 30/U, 30/U + 10$, fit for each window, compute the standard deviation of the three resulting diffusion coefficients, and plot the result as error bars.

Figure 4 shows the resulting diffusion coefficients for $U = 0.3$ as a function of the artificial decay γ. We show both FDAOE and DAOE at a variety of l_*, w_*. In each case, we linearly extrapolate the smallest two points ($\gamma = 0.05, 0.1$) to $\gamma = 0$. We extrapolate each fit window separately; the point and error bar in the FDAOE extrapolation, like the point and error bar in each of the finite-γ points, show the mean and standard deviation across the three fit windows. The DAOE diffusion coefficients are not converged in l_*, in the sense that different l_* give different extrapolations to $\gamma = 0$; this indicates that DAOE is not in the perturbative small-γ regime.

The FDAOE diffusion coefficients are converged in w_* in the sense that the error bars in the extrapolation to $\gamma = 0$ overlap: the difference between $w_* = 4$ and 5 is less than the fit uncertainty. In judging convergence, it is important to note that in simulations of $\varepsilon_x(t)$, FDAOE with these two w_*

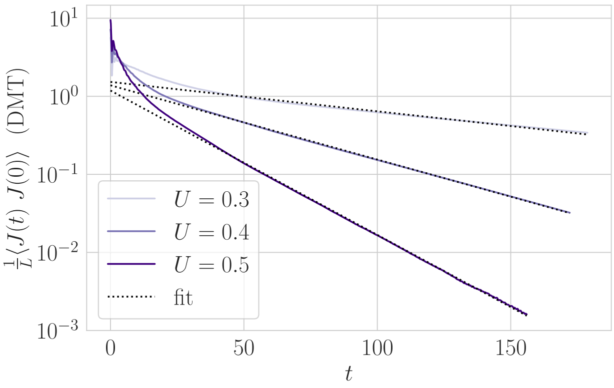

FIG. 4. Diffusion coefficients extracted from $D(t)$ via fit to exponential form (33) in FDAOE (blue lines, labeled “F” in the legend) and DAOE (yellow-red lines, labeled “D” in the legend). DAOE does not give consistent results across l_*, even when extrapolated to $\gamma = 0$, indicating that it cannot capture the crossover from free-fermion to diffusive dynamics. FDAOE gives consistent results across w_*; the diffusion coefficients extrapolated to $\gamma = 0$ are $D_{w_*=4} = 95$, $D_{w_*=5} = 89$, against a DMT value $D_{\mathrm{DMT}} = 102$. Error bars indicate uncertainty resulting from the choice of fit window; they do not include uncertainty due to Trotter or truncation error.

in fact leave the same operator Hilbert space untouched. Because the Hamiltonian and the energy density are both fermion parity even, $\varepsilon_x(t)$ is also fermion parity even, and the lowest-weight operators that suffer dissipation have weight $w = 6$, regardless of whether $w_* = 4$ or 5. ($w_* = 6$ simulations were prohibitively time-consuming.)

The FDAOE diffusion coefficients also broadly agree with the DMT simulations (black dots in Fig. 4) and in Fig. 1. The error bars do not all overlap, meaning the difference between DMT, FDAOE at $w_* = 4$, and FDAOE at $w_* = 5$ is not within fit uncertainty. But the fit is not the only source of uncertainty; DMT also has some error due to bond dimension convergence, FDAOE has some error due to SVD cutoff, and both methods have uncertainty due to (different) Trotter decompositions. (See Appendix B for other interaction strengths and some convergence data, and Appendixes C and D for discussions of convergence.) The fit to $D(t)$ seems to be more sensitive to convergence error than $D(t)$ itself.

Figure 4 shows that the diffusion coefficient is approximately linear in γ for $\gamma \lesssim 0.15$. This, together with (broad) agreement between the different w_* and agreement between FDAOE and DMT, suggests that we can treat the FDAOE superoperator perturbatively, although a rigorous justification for such a perturbative treatment is lacking.

The premise of FDAOE is that weak dissipation restricted to many-fermion operators will reduce simulation complexity, while changing transport properties in a controlled way, which can safely be extrapolated to the limit of zero projection. Figure 4 establishes that the change in transport properties is controlled, but not that simulation complexity is decreased.

Simulation complexity is controlled by bond dimension; Fig. 5 shows the maximum bond dimension as a function of time for $U = 0.4$, $w_* = 5$. The bond dimension displays a fast initial rise followed by a slow decay, as occurs in other examples of dissipative operator evolution [31,50]. The initial rise occurs as the operator $\varepsilon_x(t)$ spreads ballistically. The long-time decay results from a split into conserved and nonconserved operators; the nonconserved operators are destroyed by the FDAOE projection [21]. Concretely, FDAOE turns the Heisenberg dynamics into an effective Liouvillian $\mathcal{L}_{\mathrm{FDAOE}}$. This effective Liouvillian has slow eigenoperators given by the Fourier transform of the energy density and the energy current:

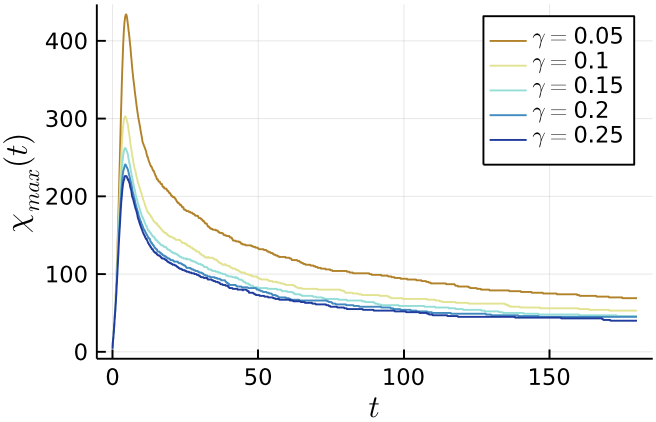

FIG. 5. Bond dimension saturation plot with $w_* = 5$ and $U = 0.4$ for various γ. We can see that the bond dimension hits the peak and falls down. Here we pick the truncation error to be 10^{-8}.

$$\mathcal{L}_{\mathrm{FDAOE}}[\tilde{\varepsilon}_k] = -iDk^2\tilde{\varepsilon}_k, \tag{35}$$

with

$$\begin{aligned} \tilde{\varepsilon}_k &= \varepsilon_k + ikDaj_k + \cdots, \\ \varepsilon_k &= \sum_x e^{ikx}\varepsilon_x, \\ j_k &= \sum_x e^{ikx} j_x. \end{aligned} \tag{36}$$

Here a is a constant related to the normalization of ε_k and j_k. At long times, then, $\varepsilon_x(t)$ becomes a sum of these Fourier modes; performing an inverse Fourier transform, it becomes

$$\varepsilon_0(t) = \sum_x [\beta(x,t)\varepsilon_x + \eta(x,t)j_x + \cdots], \tag{37}$$

with in fact $\eta(x,t) \propto D\partial_x\beta(x,t)$. [This $\beta(x,t)$ is not identical to the inverse temperature of (11), but it plays a similar role.] At finite times this has small, decaying bond dimension; in the long-time limit, $\lim_{t\to\infty}\partial_x\beta(x,t) = 0$, so the bond dimension will decay to that of the Hamiltonian.

We can rephrase the argument in the picture of [21]. In that picture, the initial energy density ε_0 develops weight on other energy densities ε_x as it evolves, but it also emits nonconserved, ballistically spreading operators. In the exact unitary dynamics, these nonconserved operators would give large bond dimension. But these operators not only spread spatially but also develop large fermion weight, so FDAOE destroys them, leaving the energy density and its current.

To measure performance in a hardware- and algorithm-agnostic way, we use the time complexity of SVD truncation after application of the superoperator MPO; we call this time

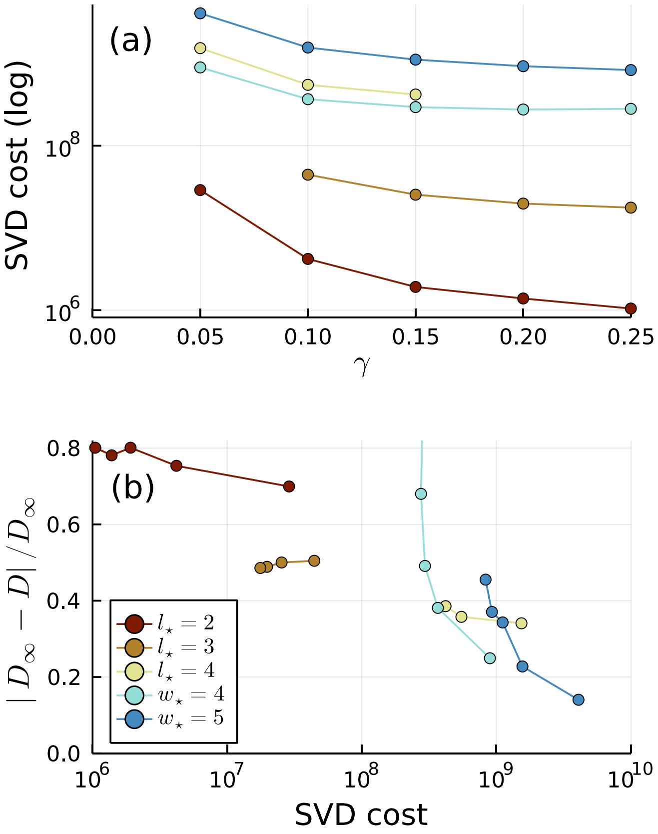

FIG. 6. (a) SVD cost with various γ for fixed $U = 0.3$ and truncation error 10^{-8}. (b) Relative error in the diffusion coefficient as a function of SVD cost. We can see that given a fixed cost, the FDAOE method has a faster convergence rate compared to DAOE.

complexity the *SVD cost*. Truncation dominates the time complexity of both DAOE and FDAOE, so the SVD cost crudely estimates the number of floating point operations needed for the simulation. Asymptotically, the time complexity of the SVD [51] at bond i is $\sim D\chi_i^3$, where D is the bond dimension of the superoperator MPO: $D = l_* + 1$ for DAOE, and $D = w_* + 2$ for FDAOE. For each method we sum over bonds at each time, and we maximize over times:

$$\text{SVD cost} = \max_t \sum_i D\chi_i(t)^3. \qquad (38)$$

Figure 6 shows the SVD cost for DAOE and FDAOE for $U = 0.3$ and a cutoff $\epsilon = 0.3$. Figure 6 (top) plots SVD cost against the artificial dissipation rate γ; it shows that—at any fixed γ—DAOE is one to two orders of magnitude cheaper.

But DAOE is not accurate: recall that DAOE gave inconsistent diffusion coefficients between lengths l_*, and that none of those diffusion coefficients agreed with DMT. FDAOE, by contrast, can be improved (at some cost in SVD time) by decreasing the artificial dissipation rate γ. Figure 6 (bottom) shows the error in the diffusion coefficient, compared to extrapolated FDAOE simulations, as a function of SVD cost. Where DAOE plateaus at some large, l_*-dependent error, FDAOE error decreases as the SVD cost increases.

V. DISCUSSION

We have presented a method, fermionic dissipation assisted operator evolution (FDAOE), for dynamics of interacting fermions in 1+1 dimensions at high temperature. FDAOE modifies a previous method, dissipation assisted operator evolution (DAOE) [31], to perform a soft truncation of operators with large fermionic weight. We tested FDAOE, DAOE, and another prior method, density matrix truncation (DMT), on an interacting Majorana model displaying *weak integrability breaking*. In weak integrability breaking, interactions dress the conserved quantities of the free model, leading to slow scattering and large diffusion coefficients. We find that FDAOE and DMT agree and give diffusion coefficients consistent with the $D \sim U^4$ scaling (U is the interaction strength), as expected from scattering of dressed fermions. We further found that FDAOE decreases the bond dimension of the MPO representation of the Heisenberg picture energy density, when combined with SVD truncation with a small error cutoff, but we also found that the small error cutoff induces noise in the time-dependent diffusion coefficient $D(t)$.

That SVD cutoff indirectly controls the uncertainties in our diffusion coefficient estimates. These uncertainties were controlled by uncertainty in the fit to the exponential form $D(t) = D - Ae^{-t/\tau}$. This fit uncertainty was driven in turn by truncation error, because we stopped the fit where truncation error [estimated by noise in $D(t)$] became appreciable. With less truncation error, we could measure $D(t)$ deeper into the exponential-decay regime, improving our estimates of the asymptotic $D = \lim_{t\to\infty} D(t)$. But most strategies for decreasing truncation error would impose substantial run-time and memory costs. Reducing the SVD cutoff, e.g., from 10^{-8} to 10^{-9}, would directly increase the bond dimension throughout the simulation, and replacing the SVD cutoff with a bond dimension cap would prevent the simulation from taking advantage of the decay of the bond dimension (Fig. 5).

But two strategies, measuring a current-current correlator and using a variable SVD cutoff—may reduce truncation error without imposing an appreciable runtime or memory cost. Estimating $D(t)$ as we do, via the mean-square displacement $V(t)$, is costly because it requires measuring $\varepsilon(x, t)$ precisely at large x. Indeed, the truncation error in $D(t)$ is $\propto \sqrt{\epsilon}\, V(t)$. Measuring a current-current correlator would avoid this problem, because the requisite spatial integral has no x^2 [unlike the integral giving $V(t)$]. Alternatively, one could use a time-varying SVD cutoff $\epsilon(t) = \epsilon_0/V(t)^2$. This would allow coarse simulations at early times, e.g., around the bond dimension peak in Fig. 5, and fine simulations at later times. Because the runtime cost contains large contributions from the bond dimension peak, this might in fact decrease runtime cost on net.

While DMT is difficult to analyze, FDAOE can be understood as a perturbative modification to the system's dynamics. This is consistent with our observation that the FDAOE diffusion coefficient is linear in the artificial dissipation γ. And the intuition is clear: at small γ, FDAOE acts weakly on few-fermion operators, and in systems that eventually thermalize, many-fermion operators are not important to transport. But establishing this formally will be nontrivial; to do so will require modifying arguments like those of [23] to work away from the strongly interacting, chaotic limit.

FDAOE is agnostic as to the details of the interaction. There are many ways to split a Hamiltonian into an unperturbed H_0 and a perturbation $\propto U$, especially if one considers nonlocal changes of basis as in [38]. As long as there exists some decomposition into a fermion-quadratic part and a small nonquadratic part, though, we expect FDAOE to work. But we expect FDAOE to work best when the nonquadratic part has no further structure, so some analog of the chaos assumption of [24] holds and the dynamics of many-fermion operators is effectively random. In this way, it is somewhat surprising that FDAOE works for the weak integrability breaking Hamiltonian, where the quasiconserved quantities provide additional structure. The fact that FDAOE reproduces the U^4 diffusion coefficients, despite having no built-in knowledge of the decomposition of [38], is a stringent test of FDAOE, and supports the natural belief that the particular decomposition of [38] governs the model's transport.

In one-dimensional fermion chains, the Jordan-Wigner transformation produces an equivalent local Hamiltonian that takes the form of a spin chain; a fermionic description of the transport is unnecessary in the generic case. For this reason, we have focused on weakly interacting systems, where transport receives important contributions from the nearly conserved quadratic fermion operators of all sizes. While the Hamiltonian can be written as a local operator in the spin language, these nearly conserved operators cannot. By contrast, in higher-dimensional fermionic systems, the energy density has no local spin representation. The dynamics of such systems can be computed using MPS by picking a one-dimensional ordering of the sites and using the Jordan-Wigner representation to convert to a spin Hamiltonian, with some terms involving nonlocal Jordan-Wigner strings. In this scenario, the DAOE superoperator will cause the energy density to decay rapidly, while the FDAOE superoperator will not. Thus, we expect that FDAOE is the appropriate choice for fermionic systems of all interaction strengths in higher dimensions.

While we focused in this paper on infinite-temperature transport, extending the methods to allow for finite-temperature calculations is needed for many physical scenarios of interest. In scenarios where the equilibrium state is dominated by quadratic fermionic operators—particularly at high temperatures with weak interactions—the FDAOE operator will only weakly perturb the equilibrium. Thus, it may still be possible in these cases to recover the correct dynamics using FDAOE with the extrapolation to zero dissipation rate. For the same reason, we expect FDAOE to accurately treat excitations over the ground state of a nearly free-fermion system—though matrix product states are a more suitable data structure at low temperature, because passing from states to density matrices or Heisenberg dynamics squares the bond dimension. We leave these questions to future studies.

Note added. We would like to bring the reader's attention to a related independent work [52].

ACKNOWLEDGMENTS

We would like to thank Federica Surace for helpful discussions about weak integrability breaking and sharing additional material related to Ref. [38]. We wish to thank Stuart Thomas, Yong-Chan Yoo, Jay Deep Sau, and Brian Swingle for helpful conversations in the context of related collaborations. E.J. and M.H. were supported by W911NF2010232, AFOSR MURI FA9550-19-1-0399, Department of Energy QSA program (DE-AC02-05CH11231), and the Minta Martin and Simons Foundation. B.W. was supported in part by the DOE ASCR Accelerated Research in Quantum Computing program (Award No. DE-SC0020312). P.L. acknowledges support from the Simons Foundation, the Harvard Quantum Initiative Postdoctoral Fellowship in Science and Engineering, and the National Science Foundation under Grant No. DMR-2245246. C.D.W. was supported by the U.S. Department of Energy (DOE), Office of Science, Office of Advanced Scientific Computing Research (ASCR) Quantum Computing Application Teams program, under fieldwork proposal number ERKJ347, DOE Quantum Systems Accelerator program DE-AC02-05CH11231, AFOSR MURI FA9550-22-1-0339, ARO Grant No. W911NF-23-1-0242, ARO Grant No. W911NF-23-1-0258, and NSF QLCI Grant No. OMA-2120757.

APPENDIX A: MATRIX PRODUCT OPERATOR REPRESENTATION OF FERMIONIC DAOE

In this Appendix, we give more details on the construction of the MPO representation of the fermionic DAOE superoperator $\mathcal{M}_{w_*,\gamma}$. As explained in Sec. III A, this construction relies on the Jordan-Wigner embedding of fermionic operators into the space of operators of qubits. This mapping maps each Pauli string—a single product of Pauli operators or the identity operator on each site—to a corresponding product of Majorana operators with 0, 1, or 2 Majorana factors at each site, up to a phase factor. Similarly, every product of Majorana operators maps to a Pauli string. As the MPO representation of the superoperator is by construction a linear superoperator, and because the Pauli string operators form a basis for the full space of operators, it is sufficient to confirm that the MPO representation has the correct action on each Pauli string.

The MPO is constructed with a constant rank-4 tensor $W_{ab}^{nn'}$, where $n, n' \in \{I, X, Y, Z\}$. To use a convenient notation, we will allow the virtual indices to take values of the form $a_s \in \{0_+, 0_-, 1_+, 1_-, \dots, w^*_+, w^*_-\}$, where the integer part of the label a is used to track a fermion weight, and the subscript s is used to track a fermion parity. There are $2(w^*+1)$ such labels—however, we will find that we only use the labels $0_+, 1_-, 2_+, 3_-, \dots$ and w^*_+, w^*_-, where for $a < w^*$ the parity label s matches the parity of a as an integer. This results in a set of w^*+2 total labels, and thus the bond dimension of our MPO representation is w^*+2.

The nonzero matrix elements of our MPO tensor $W_{ab}^{nn'}$ are as follows:

$$W^{II}_{a_+,b_+} = W^{ZZ}_{a_-,b_-} = \delta_{a,b}, \tag{A1}$$

$$\begin{aligned} W^{XX}_{a_+,b_-} &= W^{YY}_{a_+,b_-} = \delta_{a+1,b} + e^{-\gamma}\delta_{a,w^*}\delta_{b,w^*},\\ W^{XX}_{a_-,b_+} &= W^{YY}_{a_-,b_+} = \delta_{a+1,b} + e^{-\gamma}\delta_{a,w^*}\delta_{b,w^*},\\ W^{II}_{a_-,b_-} &= W^{ZZ}_{a_+,b_+} = \delta_{a+2,b} + e^{-2\gamma}\delta_{a,w^*}\delta_{b,w^*}\\ &\quad + e^{-\gamma}\delta_{a,w^*-1}\delta_{b,w^*}. \end{aligned} \tag{A2}$$

The left- and rightmost tensor in the MPO representation are to be contracted with vectors $v_a^L = \delta_{a,0_+}$ and $v_b^R = 1$ on the left and right virtual bond, respectively.

To understand this implementation of the MPO, we first note that the nonzero elements listed guarantee a consistent tracking of fermion parity. In more exact terms, the only contributions to $M_{w^*,\gamma}[O]$ for a Pauli string $O = \prod_i O_i$ occur when the parity index of the bond between site j and $j+1$ matches the fermion parity of $\prod_{i\leqslant j} O_i$ for all j. This is convenient, as matching the fermion parity allows us to determine whether the basis operator O has an even or odd number of Jordan-Wigner string factors from Eq. (20) that cross the bond $j \to j+1$.

Similarly, we can see that at all bonds the fermion weight of the virtual index must match either the fermion weight of $\prod_{i\leqslant j} O_i$ or w^*, whichever is smaller. When there are an even number of Jordan-Wigner string factors, the presence of an I in a Pauli string corresponds to a Majorana product with 0 Majorana operators on that site; if instead there are an odd number, the presence of Z does instead. This gives the first line of Eq. (A2). The second line corresponds to fermion weight 1 operators, which either increases the fermion weight counter by 1 or keeps it constant if it has reached the maximum w^*. The $e^{-\gamma}$ factor dissipates Pauli strings for each additional unit of fermion weight beyond w^*. Finally, in the last line of Eq. (A2), we have Pauli string factors that correspond to fermion weight 2 operators, which requires increasing the fermion weight counter twice or increasing it to w^* and dissipating the operator by a factor of $e^{-\gamma}$ or $e^{-2\gamma}$, depending on whether the fermion weight goes 1 or 2 units beyond w^*.

To respect the $U(1)$ charge symmetry, one need only do an on-site operator change of basis from the X, Y basis to the $X \pm iY$ basis (in the spin language). This change of basis preserves fermion parity, so there are no issues related to the Jordan-Wigner strings.

The FDAOE tensors can be shown to respect the $U(1)$ symmetry as a tensor network by assigning the $U(1)$ charges as follows: $X - iY$ is charge 1, $X + iY$ is charge -1, and I and Z are charge 0. The states on the virtual legs of the tensors are all charge 0.

To respect $U(1)$ spin symmetry (i.e., total S^z conservation), work analogously with spin. The chain with spin can be viewed as a chain with two sites per unit cell; the $X + iY$ and $X - iY$ are assigned charges that depend on whether the site corresponds to a spin-up mode (-1, 1, respectively) or a spin-down mode (1, -1 respectively).

TABLE I. Diffusion coefficients from fit to DMT $D(t)$. Mean and standard deviation are across three different fit-window end times.

U	δt	$\chi_{\max}$	D (mean)	D (std)
0.3	0.0625	128	96.8	5.7
0.3	0.125	128	106.238	14.6
0.3	0.125	256	102.367	2.38278
0.4	0.0625	128	39.4765	2.01023
0.4	0.0625	256	38.2516	0.703325
0.4	0.125	128	36.3361	0.853394
0.4	0.125	256	37.9766	0.126748
0.5	0.0625	128	21.1115	1.213
0.5	0.0625	256	21.3559	0.333348
0.5	0.125	128	20.1833	0.896041
0.5	0.125	256	20.6832	0.359822

APPENDIX B: $D(t)$ AND EXTRAPOLATION FOR OTHER INTERACTION STRENGTHS

Figure 7 shows analogs of Figs. 2 and 4 for $U = 0.4$ and 0.5. Figure 7 (top) shows $D(t)$, together with fits and (in the inset) a logarithmic difference from the $D = \lim_{t\to\infty} D(t)$ resulting from the fit, across γ. Figure 7 (bottom) shows D from fit as a function of γ, together with the extrapolation from the last two points. Table I shows diffusion coefficients from fit to DMT $D(t)$.

APPENDIX C: CONVERGENCE IN SVD CUTOFF ϵ

In simulating dynamics with FDAOE we apply Trotter gates and the FDAOE MPO; after each application, we discard small singular values

$$\sum_{\alpha\ \text{discarded}} s_\alpha^2 < \epsilon \left[\sum_\beta s_\beta^2\right]. \tag{C1}$$

Table II shows diffusion coefficients from fit to FDAOE $D(t)$. Figure 8 shows $D(t)$ for $\epsilon{=}10^{-8}$, 10^{-9} at $U{=}0.55$, $\gamma{=}0.2$.

TABLE II. Diffusion coefficients from fit to FDAOE $D(t)$. Mean and standard deviation are across three different fit-window end times.

U	w_*	D (mean)	D (std)
0.3	4.0	94.9121	4.37422
0.3	5.0	89.4662	2.67036
0.35	4.0	59.2131	3.09694
0.35	5.0	51.6491	1.63505
0.4	4.0	36.2878	1.60103
0.4	5.0	35.2506	4.91012
0.45	4.0	24.3317	1.3542
0.45	5.0	25.2716	1.03157
0.5	4.0	19.8595	2.73888
0.5	5.0	20.9656	0.495984
0.55	4.0	16.4897	0.502595
0.55	5.0	15.1526	0.807459
0.6	4.0	14.0067	0.270231
0.6	5.0	13.8689	0.562507

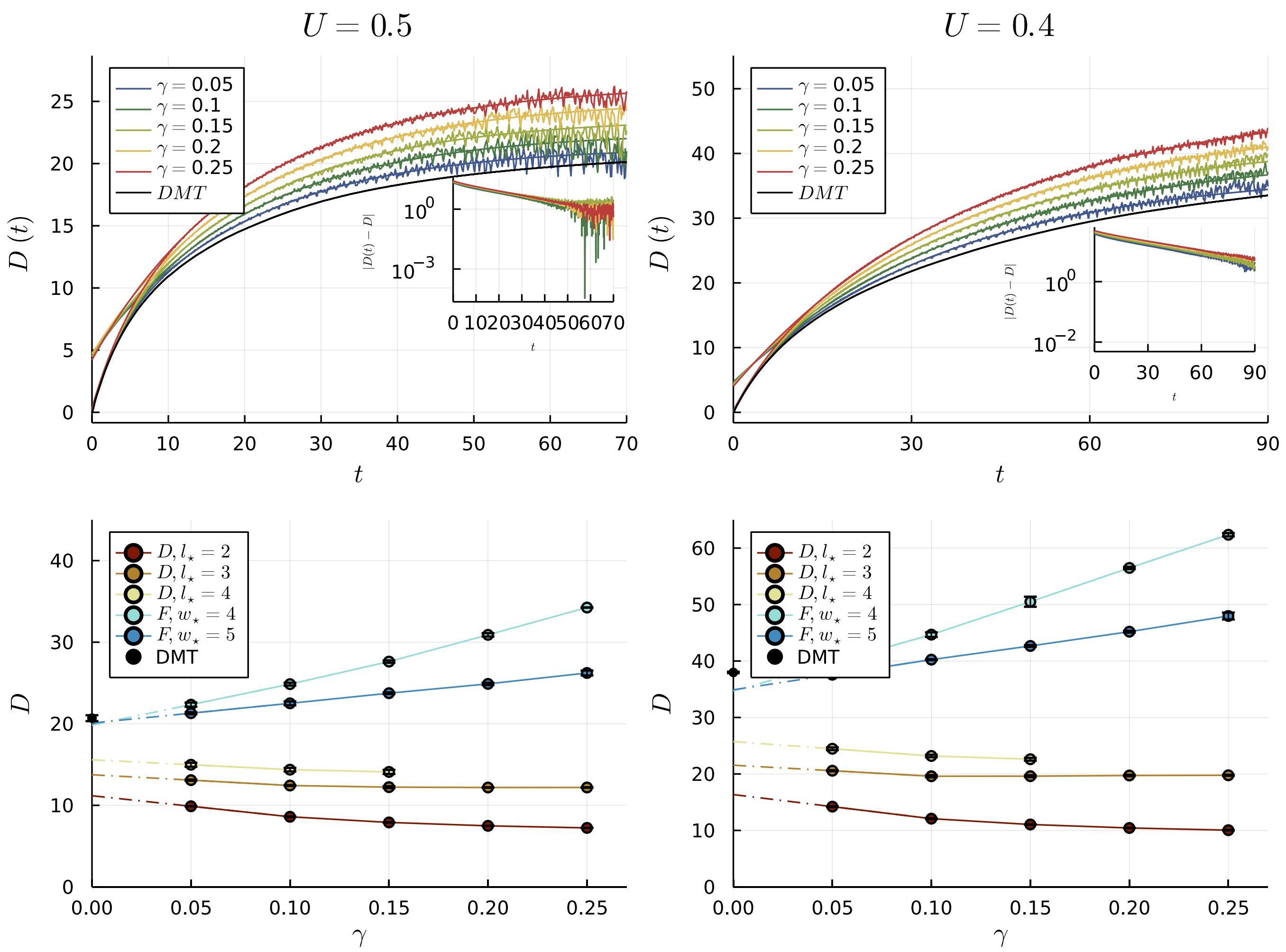

FIG. 7. Analogs of Figs. 2 and 4 for $U = 0.4$ and 0.5. The left panel is $U = 0.5$ and the right one is $U = 0.4$. All data come from Trotter step $dt = 0.1$, and the cutoff $\epsilon = 10^{-8}$.

The noise in each $D(t)$ worsens with time, and it is smaller for $\epsilon = 10^{-9}$ than for $\epsilon = 10^{-8}$. Figure 9 (top) shows the rms noise as a function of time for $U = 0.3$, $\gamma = 0.05$, $\epsilon = 10^{-8}$; there we see that it is in fact roughly proportional to the mean-square displacement $V(t)$. (We describe how we calculate the noise in Appendix C 2 below.) A heuristic *a priori* argument (Appendix C 1 below) predicts a noise magnitude

$$\Delta D_{\text{pred}}(t) = \alpha\sqrt{\epsilon}\, V(t), \tag{C2}$$

where α is a fit parameter depending (in part) on the time step δt.

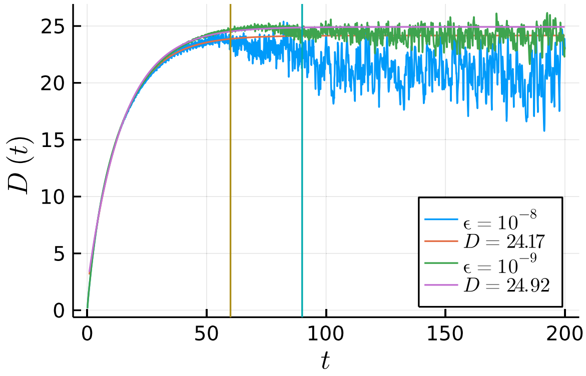

FIG. 8. We compared $D(t)$ with two truncation errors 10^{-8} and 10^{-9} with $U = 0.55$, $w_* = 4$, $\gamma = 0.2$. We also do the exponential extrapolation and see that D only differs by less than 5%.

Figure 9 shows the ratio of the measured noise magnitude ΔD_{meas} to the prediction ΔD_{pred} of (C2) for a variety of U, γ, and ϵ. For short times ($t \lesssim 25$) the ratio is large. This is in part because the prediction ΔD_{meas} is initially small, because the mean-square displacement $V(t)$ is small. Additionally, the measured noise displays a small peak at $t = 0$, already visible in Fig. 9 (top), resulting from the details of our noise measurement procedure. For $t \gtrsim 25$, the noise magnitude is reasonably well-predicted by (C2).

1. Heuristic *a priori* estimate of noise in $D(t)$ due to SVD truncation

Heuristically, the truncation applies a random perturbation of magnitude $\sqrt{\epsilon}$ to the operator truncated. When the operator truncated is the Heisenberg operator $\varepsilon_{L/2}(t)$, truncation maps

$$\varepsilon_{L/2}(t) \mapsto (1 + \sqrt{\epsilon} W)[\varepsilon_{L/2}(t)], \tag{C3}$$

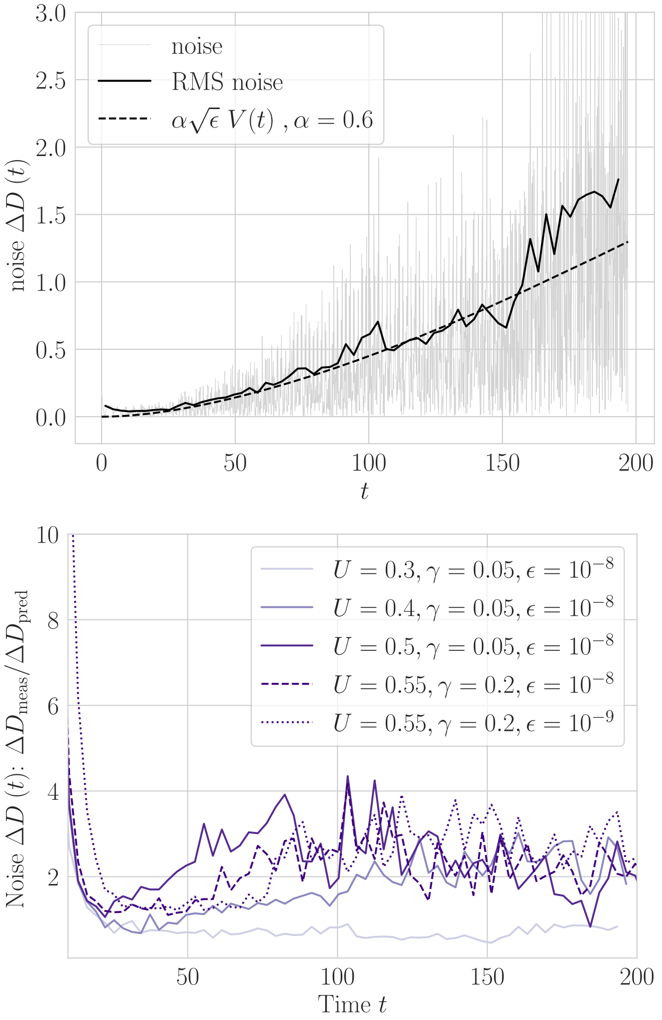

FIG. 9. Top: Noise magnitude at $U = 0.3$, $\gamma = 0.05$, $\epsilon = 10^{-8}$ compared to the prediction $\Delta D_{\mathrm{pred}}(t) = \alpha\sqrt{\epsilon}\,V(t)$ (C2), with the fit parameter α chosen by eye. Bottom: noise at a variety of U, γ, and ϵ normalized by the prediction ΔD_{pred} with $\alpha = 1$.

where V is some (not necessarily unitary) superoperator; this changes the correlation function to

$$\begin{aligned} C^{\varepsilon\varepsilon}(x,t) &= \mathrm{tr}(\varepsilon_x(1+\sqrt{\epsilon}W)[\varepsilon_{L/2}(t)]) \\ &= C^{\varepsilon\varepsilon}(x,t) + \sqrt{\epsilon}\,\mathrm{tr}(\varepsilon_x W[\varepsilon_{L/2}(t)]). \end{aligned} \tag{C4}$$

The superoperator W acts locally. To understand this, recall that $\varepsilon_{L/2}(t)$ is a low-bond dimension MPO, so it has a correlation length set by the leading nontrivial eigenvalue of the transfer matrix. Perturbations like truncation heal within that correlation length, so the superoperator W acts with a range given by that correlation length.

Since W acts locally, estimate

$$\begin{aligned} \mathrm{tr}[\varepsilon_x W \varepsilon_{L/2}(t)] &= \xi(x,t)\mathrm{tr}[\varepsilon_x \varepsilon_{L/2}(t)] \\ &\equiv \xi(x,t) C^{\varepsilon\varepsilon}(x,t), \end{aligned} \tag{C5}$$

where $\xi(x,t)$ is a random variable with

$$\langle \xi(x,t)\xi(x',t')\rangle = \alpha^2 \delta_{xx'}\delta(t-t'), \tag{C6}$$

where α is some constant. Truncation then takes

$$C^{\varepsilon\varepsilon} \mapsto [1+\sqrt{\epsilon}\,\xi(x,t)]C^{\varepsilon\varepsilon}(x,t) \tag{C7}$$

and the mean-squared displacement

$$\begin{aligned} V(t) \mapsto V'(t) &= \sum_x x^2[1+\sqrt{\epsilon}\,\xi(x,t)]C^{\varepsilon\varepsilon}(x,t) \\ &= V(t) + \Delta V_{\mathrm{trunc}}(t), \end{aligned} \tag{C8}$$

with

$$\Delta V_{\mathrm{trunc}}(t) = \sqrt{\epsilon}\sum_x x^2 C^{\varepsilon\varepsilon}(x,t)\xi(x,t). \tag{C9}$$

This truncation appears as noise in the time-dependent diffusion coefficient: the numerical derivative leading to the diffusion coefficient is

$$D(t) = \tfrac{1}{2}\delta t^{-1}[V'(t+\delta t) - V(\delta t)] \tag{C10}$$

$$= D_{\mathrm{phys}} + \tfrac{1}{2}\delta t^{-1}\Delta V_{\mathrm{trunc}}(t), \tag{C11}$$

where D_{phys} is the "physical" contribution to the numerical derivative, coming from the pre-truncation time step, and the second term $\propto \Delta V_{\mathrm{trunc}}(t)$ is the noise coming from the truncation. We can then estimate the magnitude of the noise by treating $\xi(x,t)$, hence $\Delta V_{\mathrm{trunc}}$, as random variables and estimating the variance:

$$\begin{aligned} \langle \Delta V_{\mathrm{trunc}}(t)^2\rangle &= \epsilon\left\langle\left[\sum_x x^2 C^{\varepsilon\varepsilon}(x,t)\xi(x,t)\right]^2\right\rangle \\ &= \epsilon\sum_x x^4 C^{\varepsilon\varepsilon}(x,t) \\ &= \alpha\epsilon V(t)^2 \end{aligned} \tag{C12}$$

using $\langle\xi(x,t)\xi(x',t')\rangle = \alpha\delta_{xx'}\delta(t-t')$ and sweeping some dimensionless factors into α. The standard deviation of the noise in $D(t)$ is therefore

$$\alpha\sqrt{\delta t^{-1}\epsilon/2}\,V(t). \tag{C13}$$

This expression includes a dependence on Trotter step δt coming from the numerical derivative. But the numerical derivative is not the only source of δt dependence. Consider, for example, the limit of small δt. In that limit, a Trotter step introduces only small Schmidt values, which are all discarded by truncation: that is, the truncation can undo the effect of time evolution. We do not claim to consider all sources of δt-dependence, so we sweep it into the constant α. The predicted standard deviation of the noise is then

$$\Delta D_{\mathrm{pred}} = \alpha\sqrt{\epsilon/2}\,V(t). \tag{C14}$$

Figure 9 shows the noise compared to the prediction; we see reasonable agreement.

2. Estimating the noise magnitude

We seek to estimate the noise magnitude without reference to a global fit like the exponential fit of Sec. IV. In brief, we estimate noise by binning in time, averaging $D(t)$ in each bin, constructing a linear interpolant between averages, and measuring the rms deviation from the interpolant. In more detail, we do the following:

(i) Compute variances V_j at time steps $(j-1)\delta t$, $j = 1 \dots$. (Throughout this section, $\delta t = 0.1$.)

(ii) Compute time-dependent diffusion coefficients

$$D_j = \delta t^{-1}[V_{j+1} - V_j]; \tag{C15}$$

assign them to times

$$t_j = (j - 1/2)\delta t. \tag{C16}$$

(iii) Bin and average $D(t)$ over bins of width $n = 30$, corresponding to a time window 3: that is, compute

$$\begin{aligned}\bar{D}_k &= \frac{1}{n}\sum_{j=n(k-1)+1}^{nk} D_j\\ &= (n\delta t)^{-1}[V_{nk+1} - V_{n(k-1)+1}];\end{aligned} \tag{C17}$$

assign $\bar{D}_k$ to a time

$$\bar{t}_k = (nk - 1 - n/2)\delta t. \tag{C18}$$

(iv) Form a linear interpolant $T(t)$ between the points $(\bar{t}_k, \bar{D}_k)$. (For $t < \bar{t}_1$, we linearly extrapolate.)

(v) Form errors

$$E_j = D_j - T(t_j) \tag{C19}$$

with D_j, t_j from step (ii).

(vi) Take the rms of E_j over windows of 30 points, corresponding to time windows of size 3, for ΔD_{meas}.

APPENDIX D: DMT SIMULATIONS

1. DMT

In TEBD [53–55] one truncates an MPO with a single SVD, resulting in a local approximation that is optimal with respect to the Frobenius norm. But the Frobenius norm is blind to the fact that some operators—especially local operators like energy density—are more important than others.

Density matrix truncation [30] replaces the SVD truncation with a truncation that exactly preserves operators with support up to some preservation diameter l_{pres}, and truncates longer operators via SVD; it has been successfully applied to thermalizing [30,32,35] and integrable [33,34] systems.

We implement DMT as modified in [35] for Heisenberg dynamics; for simplicity of implementation, we take a preservation diameter $L_{\mathrm{pres}} = 3$. We use a second-order boustrophedon (sweeping, DMRG-like) Trotter decomposition, rather than the usual brickwork Trotter decomposition; this seems to give better convergence in Trotter step.

2. Current decay

a. Diffusion coefficients and the current-current correlator

In the main text we extract the diffusion coefficient from the variance of the energy density correlator. That correlator is

$$C^{\varepsilon\varepsilon}(x,t) = \langle \varepsilon_x(t)\varepsilon_x(L/2)\rangle. \tag{D1}$$

TABLE III. Time constants for the phenomenological two-exponential fit [Eq. (D9)] to the current-current correlation function (D7) plotted in Fig. 10.

U	τ_1	τ_2
0.3	15.3	133
0.4	6.22	44.7
0.5	4.38	21.45

To extract a time-dependent diffusion coefficient, we first compute the mean-squared displacement

$$V(t) = \frac{1}{\nu}\sum_x x^2 C^{\varepsilon\varepsilon}(x,t) - \left(\sum_x xC(x,t)\right)^2, \tag{D2}$$

where ν is a normalization

$$\nu = \sum_x C(x,t) = \sum_x C(x,0) = \langle \varepsilon_{L/2}^2\rangle. \tag{D3}$$

The time-dependent diffusion coefficient is

$$D(t) = \frac{1}{2}\frac{d}{dt}V(t); \tag{D4}$$

we estimate this via a numerical derivative. We then estimate the physical diffusion coefficient

$$D = \lim_{t\to\infty} D(t) \tag{D5}$$

by fitting $D(t)$ to the functional form

$$D(t) = D - Be^{-t/\tau}, \quad t > t_0 \tag{D6}$$

after some initial time t_0.

It is useful to check the functional form (D6) by computing directly the derivative $\frac{d}{dt}D(t)$. We can write $\frac{d}{dt}D(t)$ as a correlator by repeatedly applying the conservation law $\partial_t \varepsilon_x = j_{x-1} - j_x$, summation by parts, time translation invariance, and spatial translation invariance to the correlator $C(x,t)$; the result is

$$\frac{d}{dt}D(t) = \frac{1}{\nu}\langle J(t)J(0)\rangle, \tag{D7}$$

where

$$J(t) = \sum_x j_x(t), \tag{D8}$$

$j_x(t)$ is the local energy current operator, and ν is the same normalization (D3).

b. Results and convergence

Figure 10 shows the current-current correlator $\langle J(t)J(0)\rangle$ as a function of time for $U = 0.3, 0.4, 0.5$. In each case, the correlator shows fast early oscillations, followed by a slow decay. The fast oscillations result from the definition of the current (see Appendix D 2 c). The slow decay is well-approximated by a phenomenological functional form

$$\langle J(t)J(0)\rangle = Ae^{-t/\tau_1} + Be^{-t/\tau_2}. \tag{D9}$$

We fit to the $t \geqslant 5$ data to avoid the initial oscillations, and give the resulting time constants τ in Table III.

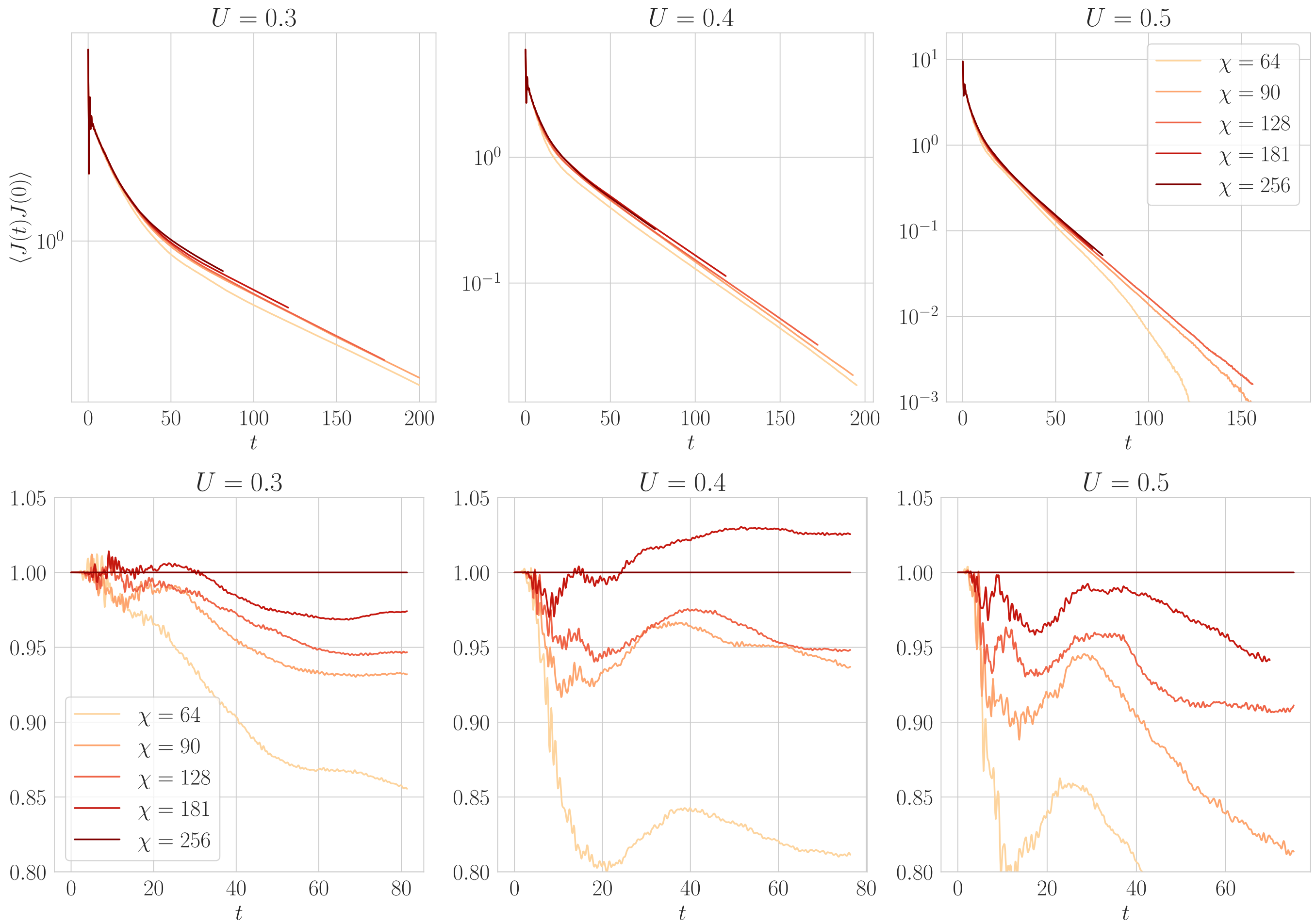

FIG. 10. Top row: current-current correlator $\langle J(t)J(0)$ of Eq. (D7) computed with DMT for $U = 0.3$ (left), $U = 0.4$ (center), and $U = 0.5$ (right). After a fast initial oscillation, the correlator displays a slow decay well approximated by a two-exponential fit [blue line, Eq. (D9)]. Bottom row: convergence in bond dimension. All curves are at Trotter step $dt = 0.125$.

Figure 10 (bottom row) shows convergence of the DMT current-current correlator in bond dimension for $U = 0.3, 0.4, 0.5$. We plot

$$\frac{\langle J(t)J(0)\rangle[\chi]}{\langle J(t)J(0)\rangle[\chi = 256]}. \tag{D10}$$

In each case, we find that $C^{JJ}_{\chi=256}(t)$ is within 10% of $C^{JJ}_{\chi=512}$.

This 10% difference understates convergence error, because $C^{JJ}_{\chi}(t)$ trends upward as the bond dimension χ increases. (The trend is unambiguous for $U = 0.3, 0.5$; for $U = 0.4$ it is less clear, but arguably still present.) It appears that DMT systematically underestimates $C^{JJ}_{\chi}(t)$. We believe this underestimate results from our choice of preservation diameter. We use DMT with preservation diameter 3, meaning it exactly preserves only those operators with support on up to three sites, but the energy current is a four-site operator. We believe that simulations with preservation diameter $\geqslant 4$ would converge more quickly.

Figure 11 shows convergence of the DMT current-current correlator in Trotter step dt. We plot

$$\frac{\langle J(t)J(0)\rangle[dt = 0.125]}{\langle J(t)J(0)\rangle[dt = 0.0625]} \tag{D11}$$

for $U = 0.3, 0.4, 0.5$; in each case the Trotter step $dt = 0.125$ is within 10% of Trotter step $dt = 0.0625$.

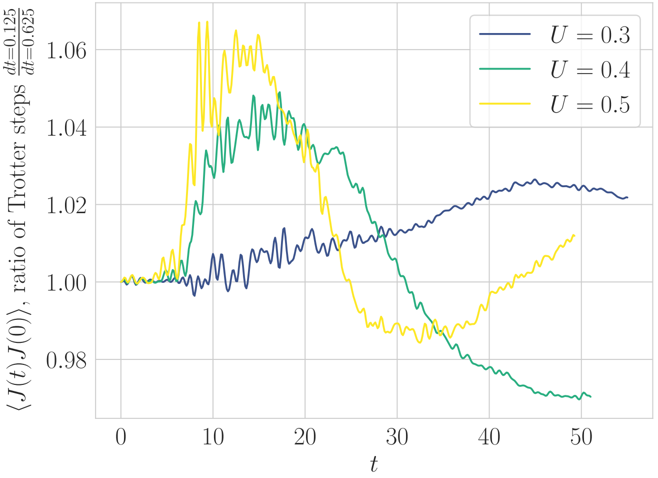

FIG. 11. Trotter step convergence of the current-current correlator in DMT simulations. Each curve is at bond dimension $\chi = 256$.

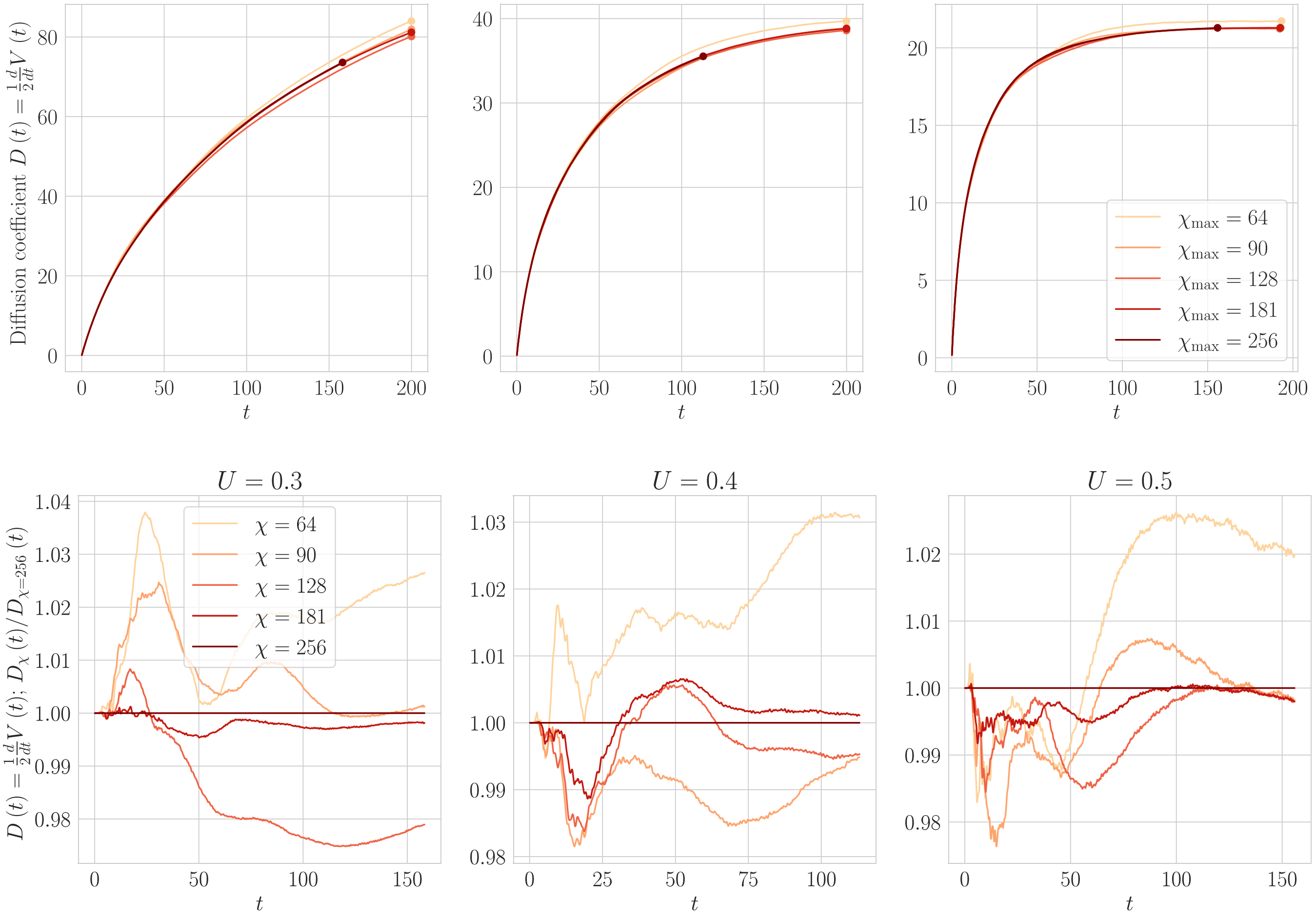

FIG. 12. Top row: time-dependent diffusion coefficients $D(t)$ extracted from DMT simulations of the mean-square displacement $V(t)$ for $U = 0.3, 0.4, 0.5$. Bottom row: bond dimension convergence of extracted $D(t)$; in each case, $D(t)$ differs between bond dimension $\chi = 64$ and bond dimension $\chi = 256$ by less than 5%. DMT simulations use Trotter step $dt = 0.125$.

c. Definitions of energy density and energy current

In this Appendix, we have used definitions of energy density and energy density current that are natural in fermion language, rather than in spin language, because the requisite analytical calculations (especially of the current itself) were more convenient in fermion language. In Majorana language, the energy density is

$$\varepsilon_\xi^{(M)} = i\eta_\xi\eta_{\xi+1} - U\eta_{\xi-1}\eta_\xi\eta_{\xi+1}\eta_{\xi+2}. \tag{D12}$$

$\varepsilon_\xi^{(M)}$ is symmetric under reflection about the bond $(\xi, \xi+1)$. The current of this energy density $\varepsilon^{(M)}$ can be written

$$\begin{aligned} j_\xi^{(M)} &= -2i[P_\xi - iU(A_{\xi-2} + A_{\xi-1} + B_{\xi-1} + B_\xi) \\ &\quad + U^2(D_{\xi-1} - C_{\xi-3} - C_{\xi-2} - C_{\xi-1})], \\ P_\xi &= \eta_\xi\eta_{\xi+2}, \\ A_\xi &= \eta_\xi\eta_{\xi+1}\eta_{\xi+2}\eta_{\xi+4}, \\ B_\xi &= \eta_\xi\eta_{\xi+2}\eta_{\xi+3}\eta_{\xi+4}, \\ C_\xi &= \eta_\xi\eta_{\xi+1}\eta_{\xi+2}\eta_{\xi+4}\eta_{\xi+5}\eta_{\xi+6}, \\ D_\xi &= \eta_\xi\eta_{\xi+4}, \end{aligned} \tag{D13}$$

where we label the Majorana sites $\xi = 2, \dots, 2L$.

In preparation for Jordan-Wigner transformation it is helpful to group sites: one grouped site x corresponds to two Majorana sites $(2x, 2x+1)$. The energy density (D12) is then

$$\begin{aligned} \varepsilon_x &= \varepsilon_{2x}^{(M)} + \varepsilon_{2x+1}^{(M)} \\ &= i\eta_{2x}\eta_{2x+1} - U\eta_{2x-1}\eta_{2x}\eta_{2x+1}\eta_{2x+2} \\ &\quad + i\eta_{2x+1}\eta_{2x+2} - U\eta_{2x}\eta_{2x+1}\eta_{2x+2}\eta_{2x+3}; \end{aligned} \tag{D14}$$

the current of this energy density can be written

$$j_x = j_{2x}^{(M)}. \tag{D15}$$

Note that the total currents are not the same:

$$J := \sum_x j_x = \sum_x j_{2x}^{(M)}, \tag{D16a}$$

$$J^{(M)} := \sum_\xi j_\xi^{(M)} = \sum_x [j_{2x}^{(M)} + j_{2x+1}^{(M)}] \neq J. \tag{D16b}$$

The difference between J and $J^{(M)}$ explains the early-time oscillations of the energy current in Fig. 10. Take $U = 0$, for simplicity. In that case, one can check

$$d_t J^{(M)} = 0. \tag{D17}$$

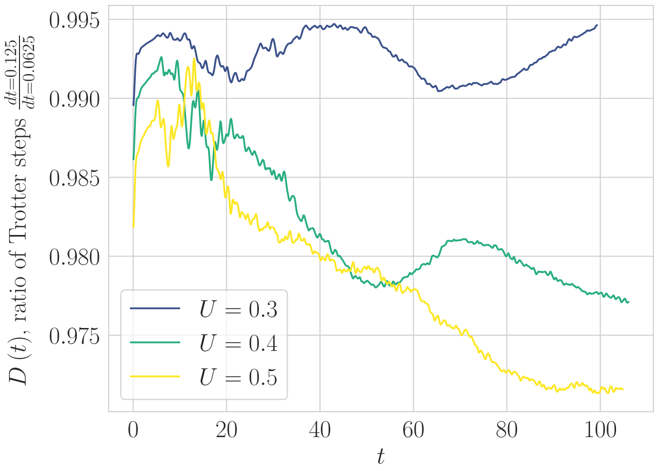

FIG. 13. Relative error between Trotter steps in diffusion coefficient extracted from DMT simulations of MSD.

If we decompose

$$J^{(M)} = J + J', \tag{D18}$$

where J is the total current of (D16a) consisting only of even terms and

$$J' = \sum_x j^{(M)}_{2x+1} \tag{D19}$$

consisting of odd terms, then $d_t J^{(M)} = 0$ implies

$$d_t J = -d_t J' \tag{D20}$$

leading to oscillations.

This is a lattice-scale phenomenon. If $U \neq 0$, for any but the shortest times $\varepsilon^{(M)}_{2x} \approx \varepsilon^{(M)}_{2x+1}$ and $j^{(M)}_{2x} \approx j^{(M)}_{2x+1}$, so the decay of J broadly matches that of $J^{(M)}$.

3. Mean-square displacement in DMT simulations

The DMT diffusion coefficients in the main text come from the mean-square displacement $V(t)$, analyzed in the same way as the FDAOE data. Figure 12 (top) shows the diffusion coefficient extracted from the mean-square displacement for $U = 0.3, 0.4, 0.5$; Fig. 12 (bottom) shows convergence in bond dimension, and Fig. 13 shows convergence in Trotter step. Bond dimension convergence error is $\lesssim 3\%$ for $\chi = 128$ compared to $\chi = 256$ (with better convergence for larger U). Trotter error is also $\lesssim 3\%$ for times $t \lesssim 90$, but growing.

[1] J. Zaanen, Planckian dissipation, minimal viscosity and the transport in cuprate strange metals, SciPost Phys. **6**, 061 (2019).

[2] J. Ayres, M. Berben, M. Čulo, Y.-T. Hsu, E. van Heumen, Y. Huang, J. Zaanen, T. Kondo, T. Takeuchi, J. R. Cooper *et al.*, Incoherent transport across the strange-metal regime of overdoped cuprates, Nature (London) **595**, 661 (2021).

[3] N. R. Poniatowski, T. Sarkar, R. P. S. M. Lobo, S. Das Sarma, and R. L. Greene, Counterexample to the conjectured Planckian bound on transport, Phys. Rev. B **104**, 235138 (2021).

[4] B. Spivak, S. V. Kravchenko, S. A. Kivelson, and X. P. A. Gao, Colloquium: Transport in strongly correlated two dimensional electron fluids, Rev. Mod. Phys. **82**, 1743 (2010).

[5] S. Kasahara, T. Shibauchi, K. Hashimoto, K. Ikada, S. Tonegawa, R. Okazaki, H. Shishido, H. Ikeda, H. Takeya, K. Hirata *et al.*, Evolution from non-Fermi-to Fermi-liquid transport via isovalent doping in $\mathrm{BaFe_2(As_{1-x}P_x)_2}$ superconductors, Phys. Rev. B **81**, 184519 (2010).

[6] S. Sachdev and B. Keimer, Quantum criticality, Phys. Today **64**, 29 (2011).

[7] A. Lucas and S. Sachdev, Memory matrix theory of magnetotransport in strange metals, Phys. Rev. B **91**, 195122 (2015).

[8] M. Stephanov, K. Rajagopal, and E. Shuryak, Signatures of the tricritical point in QCD, Phys. Rev. Lett. **81**, 4816 (1998).

[9] P. F. Kolb, J. Sollfrank, and U. Heinz, Anisotropic transverse flow and the quark-hadron phase transition, Phys. Rev. C **62**, 054909 (2000).

[10] J.-Y. Ollitrault, Anisotropy as a signature of transverse collective flow, Phys. Rev. D **46**, 229 (1992).

[11] M. M. Aggarwal *et al.* (STAR Collaboration), An experimental exploration of the QCD phase diagram: The search for the critical point and the onset of de-confinement, arXiv:1007.2613.

[12] U. Heinz, P. Sorensen, A. Deshpande, C. Gagliardi, F. Karsch, T. Lappi, Z.-E. Meziani, R. Milner, B. Muller, J. Nagle, J.-W. Qiu, K. Rajagopal, G. Roland, and R. Venugopalan, Exploring the properties of the phases of QCD matter–research opportunities and priorities for the next decade, arXiv:1501.06477.

[13] L. P. Pitaevskii and E. M. Lifshitz, *Physical Kinetics: Volume 10*, 1st ed. (Butterworth-Heinemann, Amsterdam, 1981).

[14] M. Stark and M. Kollar, Kinetic description of thermalization dynamics in weakly interacting quantum systems, arXiv:1308.1610.

[15] B. Bertini, F. H. L. Essler, S. Groha, and N. J. Robinson, Prethermalization and thermalization in models with weak integrability breaking, Phys. Rev. Lett. **115**, 180601 (2015).

[16] K. Mallayya, M. Rigol, and W. De Roeck, Prethermalization and thermalization in isolated quantum systems, Phys. Rev. X **9**, 021027 (2019).

[17] A. J. Friedman, S. Gopalakrishnan, and R. Vasseur, Diffusive hydrodynamics from integrability breaking, Phys. Rev. B **101**, 180302(R) (2020).

[18] J. Durnin, M. J. Bhaseen, and B. Doyon, Non-equilibrium dynamics and weakly broken integrability, Phys. Rev. Lett. **127**, 130601 (2021).

[19] J. Lopez-Piqueres, B. Ware, S. Gopalakrishnan, and R. Vasseur, Hydrodynamics of nonintegrable systems from a relaxation-time approximation, Phys. Rev. B **103**, L060302 (2021).

[20] J. De Nardis, S. Gopalakrishnan, R. Vasseur, and B. Ware, Stability of superdiffusion in nearly integrable spin chains, Phys. Rev. Lett. **127**, 057201 (2021).

[21] V. Khemani, A. Vishwanath, and D. A. Huse, Operator spreading and the emergence of dissipative hydrodynamics under unitary evolution with conservation laws, Phys. Rev. X **8**, 031057 (2018).

[22] T. K. Kvorning, L. Herviou, and J. H. Bardarson, Time-evolution of local information: Thermalization dynamics of local observables, SciPost Phys. **13**, 080 (2022).

[23] C. von Keyserlingk, F. Pollmann, and T. Rakovszky, Operator backflow and the classical simulation of quantum transport, Phys. Rev. B **105**, 245101 (2022).

[24] C. D. White, Effective dissipation rate in a Liouvillian-graph picture of high-temperature quantum hydrodynamics, Phys. Rev. B **107**, 094311 (2023).

[25] C. Artiaco, C. Fleckenstein, D. Aceituno, T. K. Kvorning, and J. H. Bardarson, Efficient large-scale many-body quantum dynamics via local-information time evolution, PRX Quantum **5**, 020352 (2024).

[26] P. T. Brown, D. Mitra, E. Guardado-Sanchez, R. Nourafkan, A. Reymbaut, C.-D. Hébert, S. Bergeron, A.-M. S. Tremblay, J. Kokalj, D. A. Huse, P. Schauß, and W. S. Bakr, Bad metallic transport in a cold atom Fermi-Hubbard system, Science **363**, 379 (2019).

[27] Z. Z. Yan, B. M. Spar, M. L. Prichard, S. Chi, H.-T. Wei, E. Ibarra-García-Padilla, K. R. A. Hazzard, and W. S. Bakr, A two-dimensional programmable tweezer array of fermions, Phys. Rev. Lett. **129**, 123201 (2022).

[28] J. F. Wienand, S. Karch, A. Impertro, C. Schweizer, E. McCulloch, R. Vasseur, S. Gopalakrishnan, M. Aidelsburger, and I. Bloch, Emergence of fluctuating hydrodynamics in chaotic quantum systems, arXiv:2306.11457.

[29] B. Bertini, F. Heidrich-Meisner, C. Karrasch, T. Prosen, R. Steinigeweg, and M. Znidaric, Finite-temperature transport in one-dimensional quantum lattice models, Rev. Mod. Phys. **93**, 025003 (2021).

[30] C. D. White, M. Zaletel, R. S. K. Mong, and G. Refael, Quantum dynamics of thermalizing systems, Phys. Rev. B **97**, 035127 (2018).

[31] T. Rakovszky, C. W. von Keyserlingk, and F. Pollmann, Dissipation-assisted operator evolution method for capturing hydrodynamic transport, Phys. Rev. B **105**, 075131 (2022).

[32] B. Ye, F. Machado, C. D. White, R. S. K. Mong, and N. Y. Yao, Emergent hydrodynamics in non-equilibrium quantum systems, Phys. Rev. Lett. **125**, 030601 (2020).

[33] D. Wei, A. Rubio-Abadal, B. Ye, F. Machado, J. Kemp, K. Srakaew, S. Hollerith, J. Rui, S. Gopalakrishnan, N. Y. Yao, I. Bloch, and J. Zeiher, Quantum gas microscopy of Kardar-Parisi-Zhang superdiffusion, Science **376**, 716 (2022).

[34] B. Ye, F. Machado, J. Kemp, R. B. Hutson, and N. Y. Yao, Universal Kardar-Parisi-Zhang dynamics in integrable quantum systems, Phys. Rev. Lett. **129**, 230602 (2022).

[35] S. N. Thomas, B. Ware, J. D. Sau, and C. D. White, Comparing numerical methods for hydrodynamics in a 1D lattice model, arXiv:2310.06886.

[36] Y. Li and S. C. Benjamin, Efficient variational quantum simulator incorporating active error minimization, Phys. Rev. X **7**, 021050 (2017).

[37] K. Temme, S. Bravyi, and J. M. Gambetta, Error mitigation for short-depth quantum circuits, Phys. Rev. Lett. **119**, 180509 (2017).

[38] F. M. Surace and O. Motrunich, Weak integrability breaking perturbations of integrable models, Phys. Rev. Res. **5**, 043019 (2023).

[39] A. Rahmani, X. Zhu, M. Franz, and I. Affleck, Phase diagram of the interacting Majorana chain model, Phys. Rev. B **92**, 235123 (2015).

[40] E. Leviatan, F. Pollmann, J. H. Bardarson, D. A. Huse, and E. Altman, Quantum thermalization dynamics with matrix-product states, arXiv:1702.08894.

[41] D. E. Parker, X. Cao, A. Avdoshkin, T. Scaffidi, and E. Altman, A universal operator growth hypothesis, Phys. Rev. X **9**, 041017 (2019).

[42] S. Mukerjee, V. Oganesyan, and D. Huse, Towards a statistical theory of transport by strongly-interacting lattice fermions, Phys. Rev. B **73**, 035113 (2006).

[43] L. V. Delacretaz, Heavy operators and hydrodynamic tails, SciPost Phys. **9**, 034 (2020).

[44] A. A. Michailidis, D. A. Abanin, and L. V. Delacrétaz, Corrections to diffusion in interacting quantum systems, arXiv:2310.10564.

[45] Y. Yoo, C. D. White, and B. Swingle, Open-system spin transport and operator weight dissipation in spin chains, Phys. Rev. B **107**, 115118 (2023).

[46] E. M. Stoudenmire and S. R. White, Minimally entangled typical thermal state algorithms, New J. Phys. **12**, 055026 (2010).

[47] S. Paeckel, T. Köhler, A. Swoboda, S. R. Manmana, U. Schollwöck, and C. Hubig, Time-evolution methods for matrix-product states, Ann. Phys. **411**, 167998 (2019).

[48] T. Barthel and Y. Zhang, Optimized Lie–Trotter–Suzuki decompositions for two and three non-commuting terms, Ann. Phys. **418**, 168165 (2020).

[49] ITensor svd keywords use_relative_cutoff=true, cutoff=1e-8.

[50] K. Noh, L. Jiang, and B. Fefferman, Efficient classical simulation of noisy random quantum circuits in one dimension, Quantum **4**, 318 (2020).

[51] X. Li, S. Wang, and Y. Cai, Tutorial: Complexity analysis of singular value decomposition and its variants, arXiv:1906.12085.

[52] J. Lloyd, T. Rakovszky, F. Pollmann, and C. von Keyserlingk, The ballistic to diffusive crossover in a weakly-interacting Fermi gas, arXiv:2310.16043.

[53] G. Vidal, Efficient classical simulation of slightly entangled quantum computations, Phys. Rev. Lett. **91**, 147902 (2003).

[54] G. Vidal, Efficient simulation of one-dimensional quantum many-body systems, Phys. Rev. Lett. **93**, 040502 (2004).

[55] M. Zwolak and G. Vidal, Mixed-state dynamics in one-dimensional quantum lattice systems: A time-dependent superoperator renormalization algorithm, Phys. Rev. Lett. **93**, 207205 (2004).